Chapter 9 – NUMERICAL SOLUTIONS FOR THE CAWAPI CONFIGURATION ON UNSTRUCTURED GRIDS AT USAFA, UNITED STATES

by

Scott Morton, David R. McDaniels, Russell M. Cummings

9.1 SUMMARY

This work represents the USAF Academy portion of a culmination of three years of cooperative research in the Cranked Arrow Wing Aerodynamics International (CAWAPI) RTO Task Group, AVT-113. The objective of the group was to compute high resolution CFD simulations of a subset of the conditions created in the CAWAP flight test program managed by NASA Langley researchers and others. Seven flight conditions were chosen with four of them at symmetric conditions of medium to high angle of attack and subsonic Mach numbers, one symmetric condition at a transonic low angle of attack condition, and two conditions at medium angle of attack and subsonic Mach number but with positive and negative sideslips. The emphasis of the USAF Academy team was to explore unsteady effects and the ability of current methods to predict them. Very good agreement with flight test was found in almost all cases and the unsteadiness was documented with flowfield visualization and unsteady surface pressure coefficient data.

9.2 INTRODUCTION

The Cranked-Arrow Wing Aerodynamics Project (CAWAP) provided the computational fluid dynamic (CFD) community with an excellent database for complex aerodynamic validation and verification [9-1][9-2]. A number of researchers simulated the flowfield of the F-16XL at a variety of flight test conditions using different numerical approaches, including structured, block, and unstructured grids, as well as various turbulence models and numerical algorithms. This type of full-scale aircraft configuration provides many challenges to state-of-the-art CFD flow prediction, including the ability to accurately predict unsteady flowfields at flight Reynolds numbers.

While advances have taken place in areas such as grid generation and fast algorithms for solutions of systems of equations, CFD has remained limited as a reliable tool for prediction of inherently unsteady flows at flight Reynolds numbers. Current engineering approaches to prediction of unsteady flows are based on solution of the Reynolds-averaged Navier-Stokes (RANS) equations. The turbulence models employed in RANS methods necessarily model the entire spectrum of turbulent motions. While often adequate in steady flows with no regions of reversed flow, or possibly exhibiting shallow separation, it appears inevitable that RANS turbulence models are unable to accurately predict flows characterized by massive separation. Unsteady, massively separated flows are characterized by geometry-dependent and three-dimensional turbulent eddies. These eddies, arguably, are what defeat RANS turbulence models from predicting flows of any complexity.

To overcome the deficiencies of RANS models for predicting massively separated flows, Spalart et al. [9-3] proposed Detached-Eddy Simulation (DES) with the objective of developing a numerically feasible and accurate approach combining the most favorable elements of RANS models and Large Eddy Simulation (LES). The primary advantage of DES is that it can be applied at high Reynolds numbers, as can Reynolds-averaged techniques, but DES also resolves geometry-dependent, unsteady three-dimensional turbulent

motions as in LES. The unstructured finite-volume solver Cobalt [9-4] has been used in conjunction with DES successfully on a number of complex problems, including a supersonic base flow [9-5], delta wing vortex breakdown [9-6][9-7], the F-15E at high angle of attack [9-8], the F/A-18E with unsteady shock buffet [9-9], and the F/A-18C with tail buffet [9-10].

The specific aim of this work is to perform time accurate calculations for flow over the F-16XL at full-scale flight Reynolds numbers, and to document the effects of applying DES at conditions consistent with complex flow phenomenon. Understanding the unsteady flowfield can lead to improved knowledge about the flight characteristics of aircraft that can be overlooked by steady RANS or unsteady RANS (URANS) calculations. While unsteady CFD predictions of full-scale aircraft are relatively expensive to perform, their value has been shown to be important in many of the studies referenced above. Abrupt wing stall [9-9], for example, could not have been predicted using a URANS CFD approach, and the aerodynamics of maneuvering aircraft cannot be adequately predicted without the use of a hybrid RANS/LES approach. A brief overview of the turbulence models and numerical methods used is presented, as is a detailed look at the determination of the appropriate time steps for the unsteady calculations. Results show that there are several flow features of the F-16XL that are predicted correctly using an unsteady approach.

9.3 SOLUTION METHOD

9.3.1 Flow Solver

Computations were performed using the commercial flow solver *Cobalt* [9-4]. *Cobalt* is a cell-centered, finite volume CFD code. It solves the unsteady, three-dimensional, compressible Reynolds Averaged Navier-Stokes (RANS) equations on hybrid unstructured grids. Its foundation is based on Godunov's first-order accurate, exact Riemann solver. Second-order spatial accuracy is obtained through a Least Squares Reconstruction. A Newton sub-iteration method is used in the solution of the system of equations to improve time accuracy of the point-implicit method. Strang et al [9-4] validated the numerical method on a number of problems, including the Spalart-Allmaras model, which forms the core for the Detached Eddy Simulation (DES) model available in *Cobalt*. Tomaro et al [9-11] converted the code from explicit to implicit, enabling CFL numbers as high as 10^6. Grismer et al [9-12] parallelized the code, with a demonstrated linear speed-up on as many as 4,000 processors. The parallel Metis (ParMetis) domain decomposition library of Karypis et al [9-13] is also incorporated into *Cobalt*. New capabilities include rigid-body and 6 DOF motion, equilibrium air physics, and overset grids. A coupled aeroelastic simulation capability is also being developed.

9.3.2 Numerical Grid and Boundary Conditions

The baseline unstructured grid was generated by researchers at the NASA Langley Research Center using the grid generation packages *GRIDTOOL* [9-14] and *VGRIDNS* [9-15]. The grid is a half-span all-tetrahedral mesh with a viscous inner region made up of high aspect ratio cells and a nearly isotropic outer inviscid region. The grid has 2,534,132 nodes and 14,802,429 cells and is based on a CAD representation of the full-scale model of the F-16XL-1 with all control surfaces set to zero deflection. The surface of the half-span model of the F-16XL is discretized with 160,266 triangular elements (see Figure 9-1).

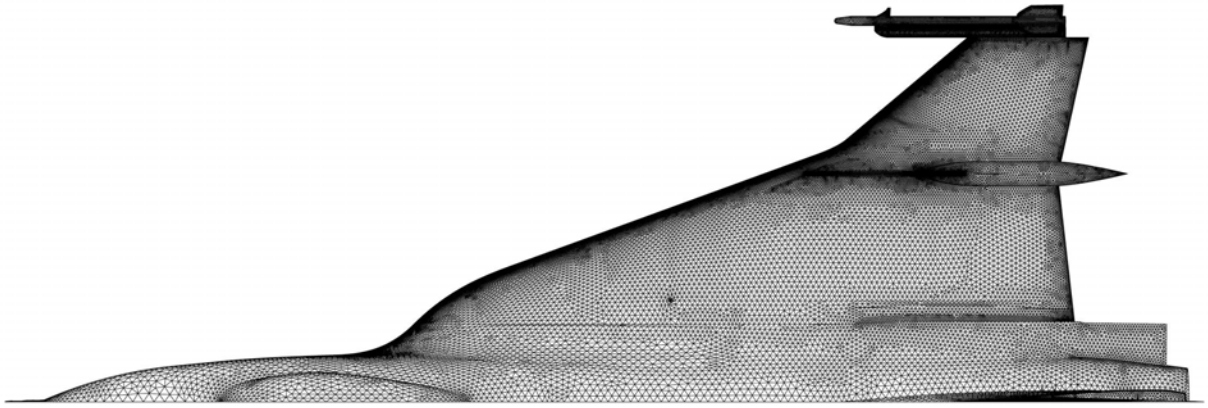

Figure 9-1: F-16XL-1 Half-Span Model Surface Grid (160,266 Faces).

Many flow solvers require the initial layers of cells off of the surface to be prisms or hexahedra to improve numerics. The all tetrahedral grid was converted to a hybrid mesh with inner layers of prisms by recombining the highly stretched inner layers of tetrahedra into prisms. The software used to convert the initial mesh into a hybrid grid was the utility program *BLACKSMITH* [9-16] from Cobalt Solutions, LLC. *BLACKSMITH* reduced the cell count to a total of 11,928,103, corresponding to 2,535,842 nodes, by combining highly stretched tetrahedral cells into prismatic cells. The program generated 9 layers of prismatic cells, corresponding to 1,442,394 prisms. Although there are additional layers of cells in the viscous region, these layers are not complete around the entire aircraft and would require "end caps" of pyramids to match up with the tetrahedral cells of the outer region.

To allow simulation of engine effects at the inlet and nozzle exit, the engine duct is meshed all the way to the compressor face plane and the nozzle is meshed from the engine mixing plane (see Figure 9-2). The grid density off the aircraft surface is shown in Figure 9-3, which depicts a crinkle cutting plane through the grid at FS496 close to the trailing edge.

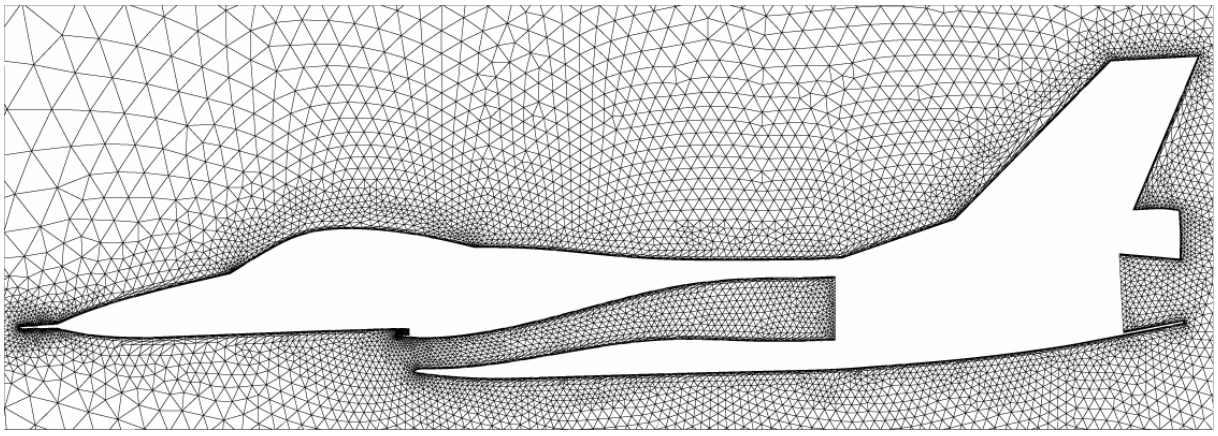

Figure 9-2: Symmetry Plane of the F-16XL-1 Baseline Unstructured Grid.

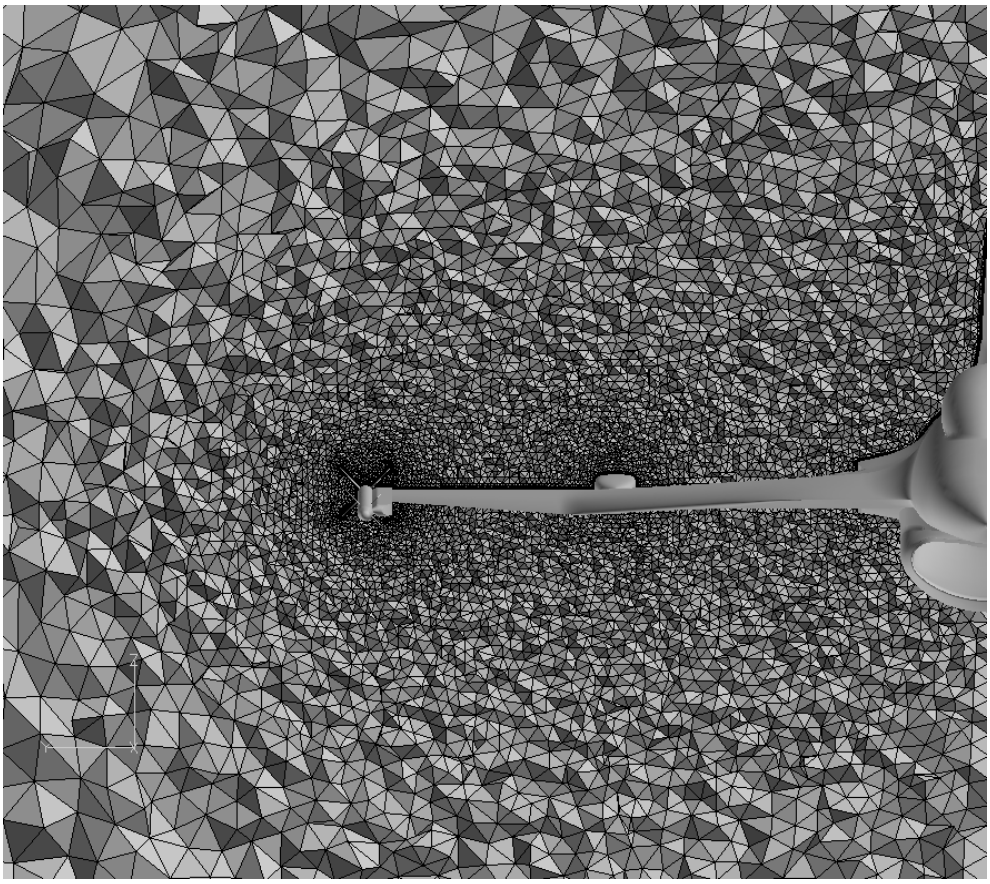

**Figure 9-3: Crinkle Cut Plane through the Grid at FS496
(Fuselage Station on Airplane in Inches, Positive Aft).**

The boundary conditions for the half-span computations are symmetry, adiabatic solid wall for the aircraft surface and the engine inlet duct, and modified Riemann invariants for the far-field boundaries. A source boundary condition based on Riemann invariants is used to create an inflow condition at the engine exhaust. A sink boundary condition is used at the engine compressor face to model the mass flow into the engine.

9.4 RESULTS

There are seven CAWAP flight conditions chosen by the CAWAPI RTO Task Group as candidates for comparison (summarized in Table 9-1). Flight conditions 7, 19, 25, 46, and 70 are assumed to be symmetric conditions and only half-span grids are used in the computations, although there is up to a +0.725 and -0.133 degree sideslip error in the assumption as noted in Table 9-1. Flight conditions 7, 19, and 46 are medium angle-of-attack conditions at various subsonic Mach numbers and altitudes, whereas, flight condition 70 is a low angle of attack condition at a transonic Mach number of 0.97. Although the Reynolds number essentially doubles (to 88.8 million) for flight condition 70, the normal spacing of the grid points above the surface in the viscous region is still within a y+ of one for the grid developed for all of the flight conditions. Flight conditions 50 and 51 are medium angle-of-attack conditions at sideslips of +5.31 and -4.58 degrees, respectively, and a mirrored full-span grid created from the baseline grid was used.

Table 9-1: Subset of CAWAP Flight Conditions Chosen for CAWAPI

CAWAPI Flight Conditions						
FC#	Mach	Altitude (ft)	AOA (deg)	Beta Actual (deg)	Beta Comp (deg)	Re#
7	0.304	5,000	11.89	-0.133	0	4.44E+07
19	0.36	10,000	11.85	0.612	0	4.68E+07
25	0.242	10,000	19.84	0.725	0	3.22E+07
46	0.527	24,000	10.4	0.684	0	4.69E+07
70	0.97	22,300	4.37	0.310	0	8.88E+07
50	0.434	24,000	13.56	5.310	5.31	3.94E+07
51	0.441	24,000	12.89	-4.580	-4.58	3.90E+07

All solutions were computed using the software *Cobalt* version 3.0 from Cobalt Solution L.L.C. installed on the Department of Defense High Performance Computing Modernization Program computer systems. Steady-state solutions and initiation of time-accurate solutions were computed using the Reynolds-Averaged Navier-Stokes (RANS) turbulence model of Spalart-Allmaras with Rotation Corrections (SARC), 1st order-accuracy in time, and a time step commensurate with a CFL number of one million. Time accurate solutions were computed with the Detached-Eddy Simulation hybrid RANS-Large Eddy Simulation turbulence model with SARC as the underlying RANS model. A time-step study was conducted to determine the proper time step for the flight condition and grid combination used for this study and is the subject of the next section.

All of the computations were run on 128 to 256 CPUs on two different supercomputing systems at the Aeronautical Systems Center Major Shared Resource Center (ASC MSRC) at Wright-Patterson Air Force Base in Ohio. The initial solutions (mainly FC7) were accomplished on "hpc9", a Compaq SC-45 with 836 Alpha EV6.8 processors running at 1 GHz and running the True64 UNIX operating system. A total of 836 GB of distributed memory was available, and each processor has access to 8 TB of hard disk space. This machine was decommissioned on September 30th, 2006. The balance of the solutions were accomplished on "falcon", a 2,048-processor AMD Opteron (2.8 GHz) cluster with 1,024 XC Compute Nodes (2 processors/node) connected with Infiniband Interconnect. Each node has 4GB of memory (4TB total) with access to 97 TB of local disk space. The machine has a peak performance of 11.5 TeraFLOPS.

Nominally, each solution (corresponding to a flight condition from Table 9-1) was initialized by accomplishing 3,000 flow solution iterations with 2nd order spatial accuracy, 1st order time accuracy with the time step size determined by the global minimum CFL number, and 1 Newton subiteration per time step. For the half-span solutions, this required 17.6 seconds per iteration on hpc9 (880 CPU hrs, 6.88 hrs of wall clock time on 128 procs) and 10.2 seconds per iteration on falcon (510 CPU hrs, 3.98 hrs of wall clock time on 128 procs). From these initial solutions, at least 6,000 additional iterations were performed with a specified time step size and 2nd order spatial and temporal accuracy with 3 Newton subiterations. These runs required 38.9 seconds per iteration on hpc9 and 20.9 seconds per iteration on falcon for the half-span solutions. The full span solutions (FC50/51) required 42.3 seconds per iteration on falcon. These timings varied depending on whether or not time-accurate flow solution files were requested. Typically, the last 2,000 iterations of each run were time-averaged to compute the average solution values in the results, and time-accurate flow solution files were exported every

5 time steps during this time period. The unsteady bounds shown in the results were determined by interrogating these flow solution files.

There are several major features of the F-16XL that contribute to the aerodynamic phenomena to be discussed in this section. The wing is a cranked arrow wing with a leading edge sweep of 70 degrees prior to the crank and 50 degrees in the post crank outer wing region. The wing leading edge is blended to the fuselage with an s-curve shape to aid in high angle of attack pitch characteristics [9-1]. There is also an actuator pod just inboard of the crank and an air dam protruding forward of the actuator pod. Finally, there is an AIM-9 missile attached to the wing-tip pylon.

In the subsequent sections, data will be presented with the nomenclature of butt line (BL) and fuselage stations (FS). The coordinate system used for analyzing the flight and CFD data is x measured aft, y measured out the right wing, and z measured up, with an origin near the nose of the aircraft. The BL is an x-z plane at a constant y coordinate and the numerical designation gives the distance from the symmetry plane to the BL plane measured in inches. The FS is a y-z plane at a constant x coordinate and the numerical designation gives the distance from the nose region to the FS plane measured in inches.

9.4.1 Time Step Study

In order to accurately predict unsteady flows about the F-16XL, both a good grid and a proper time step is required. Of course, "good" and "proper" are relative terms that need to be examined in light of the flow features of interest. If the computation is trying to resolve vortical flow features, the grid of a particular fineness coupled with a specific time step may be adequate. If the computation is trying to resolve smaller turbulent structures, then a finer grid with a smaller time step may be necessary. Figure 9-4 shows the various Strouhal numbers (dimensionless frequency defined as Sn = fc/U∞) that regularly occur in aerodynamic flowfields [9-17], which can aid in finding a good "starting" time step, based on the flow feature of interest.

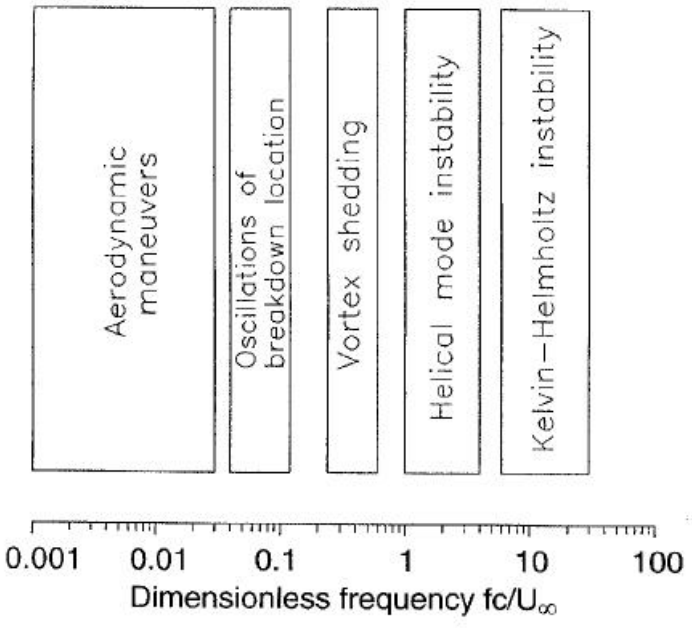

Figure 9-4: Spectrum of Unsteady Flow Phenomena (Ref. [9-17]).

In order to determine the appropriate time step for the numerical simulations of the F-16XL, a study was carried out for the unsteady flowfield above the wing. Figure 9-5 shows the variation of power spectral density of the normal force on the aircraft as a function of time at seven time steps, Δt = 0.00500, 0.00250, 0.00100, 0.00050, 0.00010, and 0.00005 seconds. These time steps were chosen based on the rule of thumb that aerodynamic features of interest are usually "visible" at non-dimensional time steps of approximately $\Delta t^* = 0.01$ ($\Delta t^* = \Delta t\, U_\infty / c$).

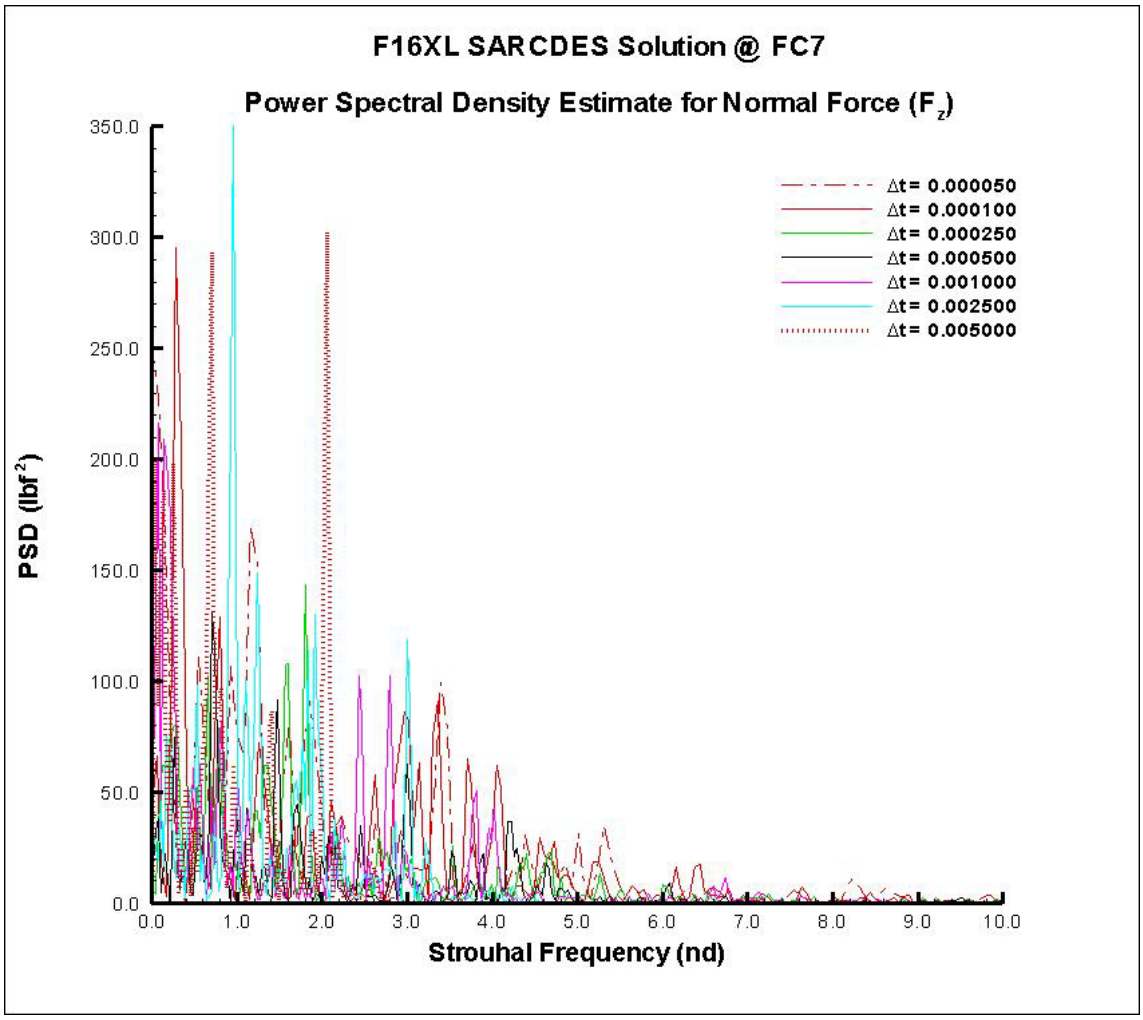

Figure 9-5: PSD of Normal Force Variation with Time at Various Time Steps.

The computations were all performed for the same physical time (1.0 second) by varying the number of iterations for each time step, and each computation was completed with three Newton sub-iterations. An additional side study was accomplished at a time step of 0.005 seconds to determine if simulating the flow field for a longer physical time (up to 3.0 seconds) affected the frequency content of the flow. No significant changes in the power spectral density results were evident. As shown in Figure 9-5, the resulting dominant Strouhal number does not show a definite trend with time step: if the dominant frequency were "converging" with decreasing time step then a lower time step would be required. However, in this case, there is no definite

trend with time step. Based on our experience in predicting these flows [9-18], this trend leads to the conclusion that the integrated normal force is "masking" a number of different flow features that are all contributing to the frequency content shown in Figure 9-5 (multiple vortices, possible vortex breakdown, flow separation regions, etc.). Because of this, we have found that taking detailed flow "measurements" within the flowfield region of interest is the only way to properly determine the primary frequencies and appropriate time steps. Therefore, a series of "pressure taps" were located in the flow, as shown in Figure 9-6, as well as Table 9-2. Figure 9-6 shows the complexity of the flowfield in the region of interest, where a primary leading-edge vortex intersects with the air dam vortex, as well as the creation of another leading-edge vortex at the wing crank. Figure 9-4 shows the pressure tap locations used in the time step study.

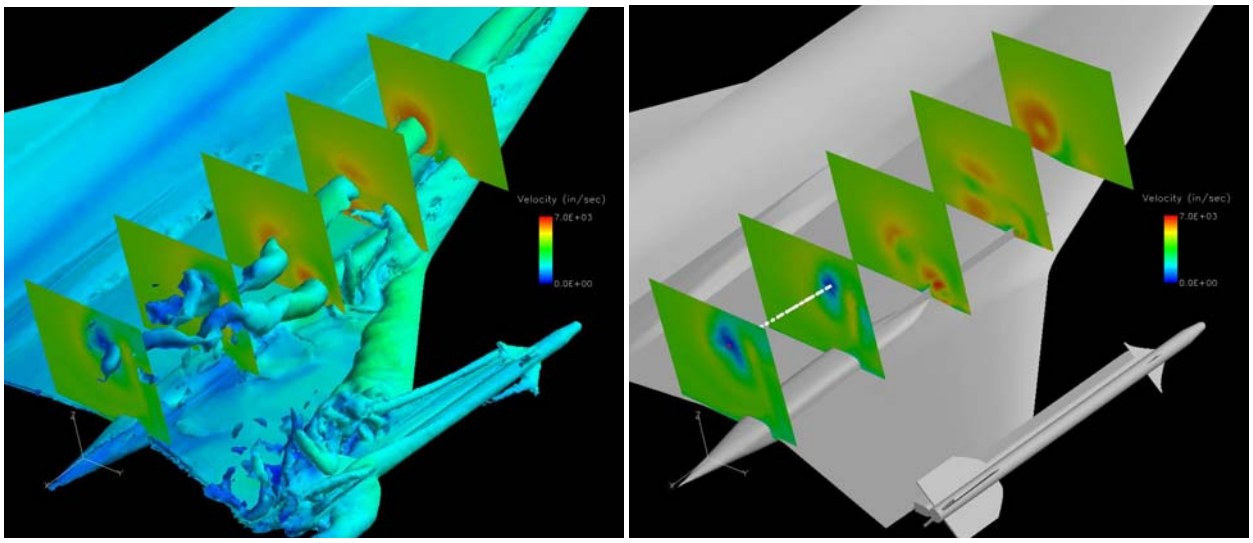

(a) **(b)**

Figure 9-6: (a) Iso-Surfaces of X-Vorticity and Velocity Cutting Planes; (b) Velocity Cutting Planes and Pressure Tap Locations (white dots).

Table 9-2: Pressure Tap Location in Region of Interest

Tap #	X (in)	Y (in)	Z (in)
1	470	124	125
2	475.39	123.326	125.135
3	480.11	122.736	125.253
4	484.941	122.132	125.374
5	491.13	121.359	125.528
6	495.509	120.811	125.638
7	499.788	120.277	125.745
8	504.74	119.657	125.869
9	510	119	126

Each time step was run with the pressure tap locations "collecting" data as a function of time. These pressures were then used to perform PSD calculations for each time step. A representative set of results is shown in Figure 9-7, which is the power spectral density at pressure tap #1. As can be seen, as the time step is decreased, the primary frequency begins to take place at a common frequency, which we consider time step "convergence." Similar results take place at pressure tap #2, but as the more aft pressure taps were evaluated, the flow became much less coherent, without any obvious primary frequencies (as can be seen in Figure 9-7 for tap #1).

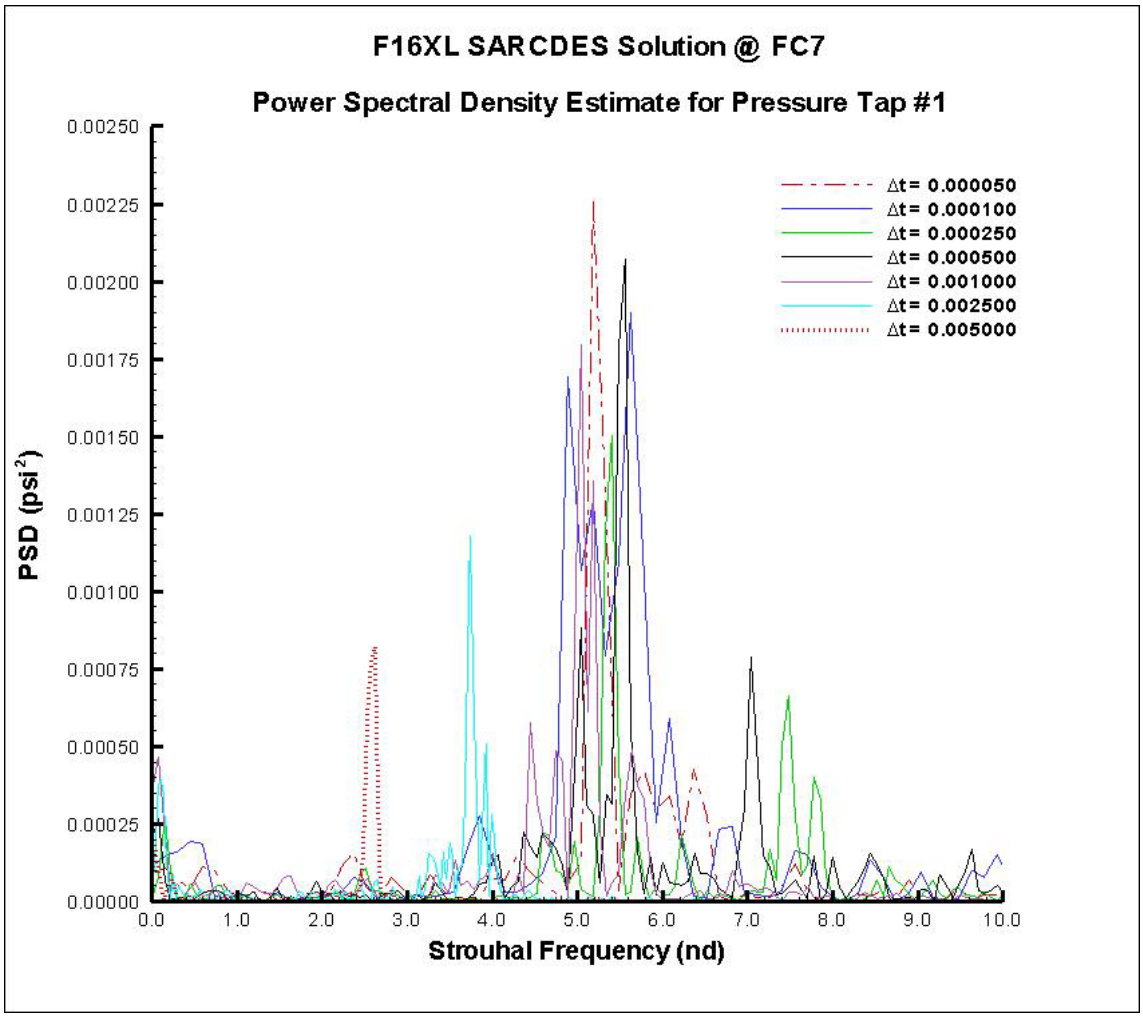

Figure 9-7: Power Spectral Density Results for Pressure Tap #1.

The results for pressure tap #1 are consolidated and shown as a function of time step and wave number in Figure 9-8. As can be clearly seen, the primary wave number is converging to a constant value as the time step decreases, with a wave number of approximately 0.19 reached when the physical time step is below $\Delta t = 0.001$ sec. While a converged time step has been attained at $\Delta t = 0.001$ sec, a smaller time step may be desirable for accurate flow prediction. It is also clear that the Strouhal frequency for the primary flow feature is somewhere in the range of 5, which corresponds to a helical mode instability in Figure 9-4.

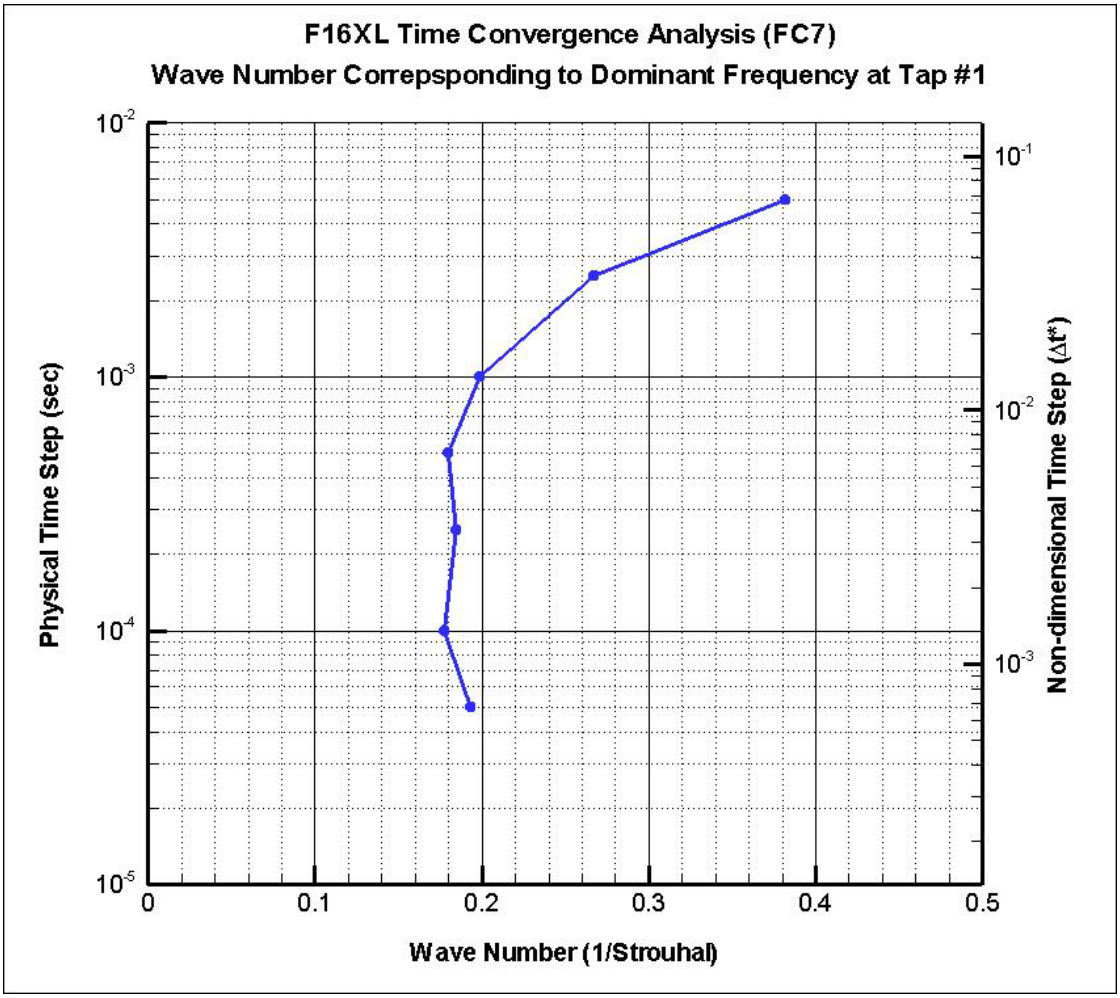

Figure 9-8: Wave Number Variation with Time Step for Pressure Tap #1.

While an additional time study could be performed to determine the effect of the number of Newton sub-iterations on the solution, our experience [9-18] shows that 3 Newton sub-iterations is usually sufficient for accurate prediction of the unsteady flows about full-scale aircraft. All subsequent calculations are performed with a physical time step of $\Delta t = 0.0005$ seconds and 3 Newton sub-iterations.

9.4.2 Low Speed Medium to High Alpha Flight Conditions

There are four flight conditions with angles of attack greater than 10 degrees and subsonic Mach numbers. Three of the flight conditions are considered a medium angle of attack in the range 10 to 12 degrees (FC7, FC19, and FC46). The fourth condition, FC25, is considered a high angle of attack condition at 19.84 degrees. This section presents results for these four flight conditions.

9.4.2.1 Flight Condition 7

Flight Condition 7 (FC7) is at an angle of attack of 11.89 degrees, a Mach number of 0.304, and an altitude of 5,000 ft resulting in a Reynolds number of 44.4 million. This condition was used by the CAWAPI RTO Task

Group as an initial comparison case between the various research teams. Unfortunately, this particular case had no flight test data to use for comparison, although there were two flight conditions close enough to be considered comparable from Flight 44 with approximately the same angle of attack and Mach numbers of 0.37 and 0.42.

Figure 9-9 depicts the flowfield over the F-16XL at FC7. Iso-surfaces of vorticity magnitude of 250 1/sec colored by pressure are shown in the perspective view and surface C_p for the right wing are shown in the planform view. It is apparent that the dominant features of the flowfield are the leading edge vortex, the air dam vortex, the outer wing vortex, and a complicated set of vortices from the AIM-9 fins and fore-body. It can also be seen that the leading-edge vortex changes characteristic from a coherent structure to a complex structure with helical windings, similar to vortex breakdown, in the region of the actuator pod. It is also interesting to note that the helical vortex structure is above the vortex emanating from the air dam creating a very complex structure. Figure 9-10 shows a close up view of this region for an iso-surface of vorticity-magnitude level of 750 1/sec with labels for the dominant features. The approximate breakdown position of the leading-edge vortex is FS470.

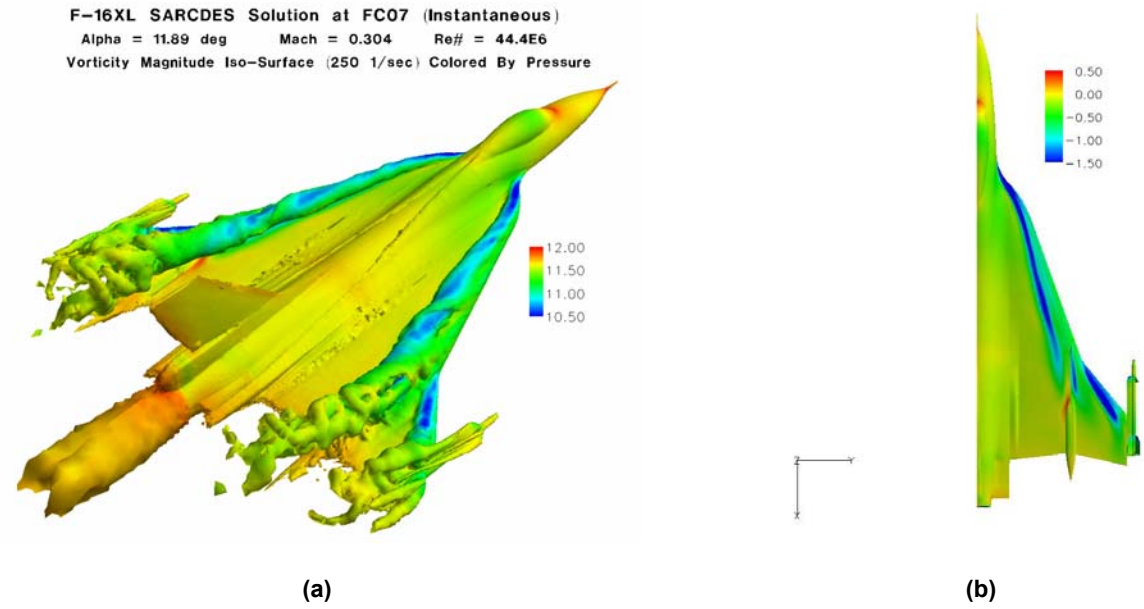

(a) (b)

Figure 9-9: Flight Condition 7: (a) Iso-Surfaces of Vorticity Magnitude Colored by Pressure at an Instant in Time; (b) Time Averaged Surface Pressure Coefficient Distribution, C_p.

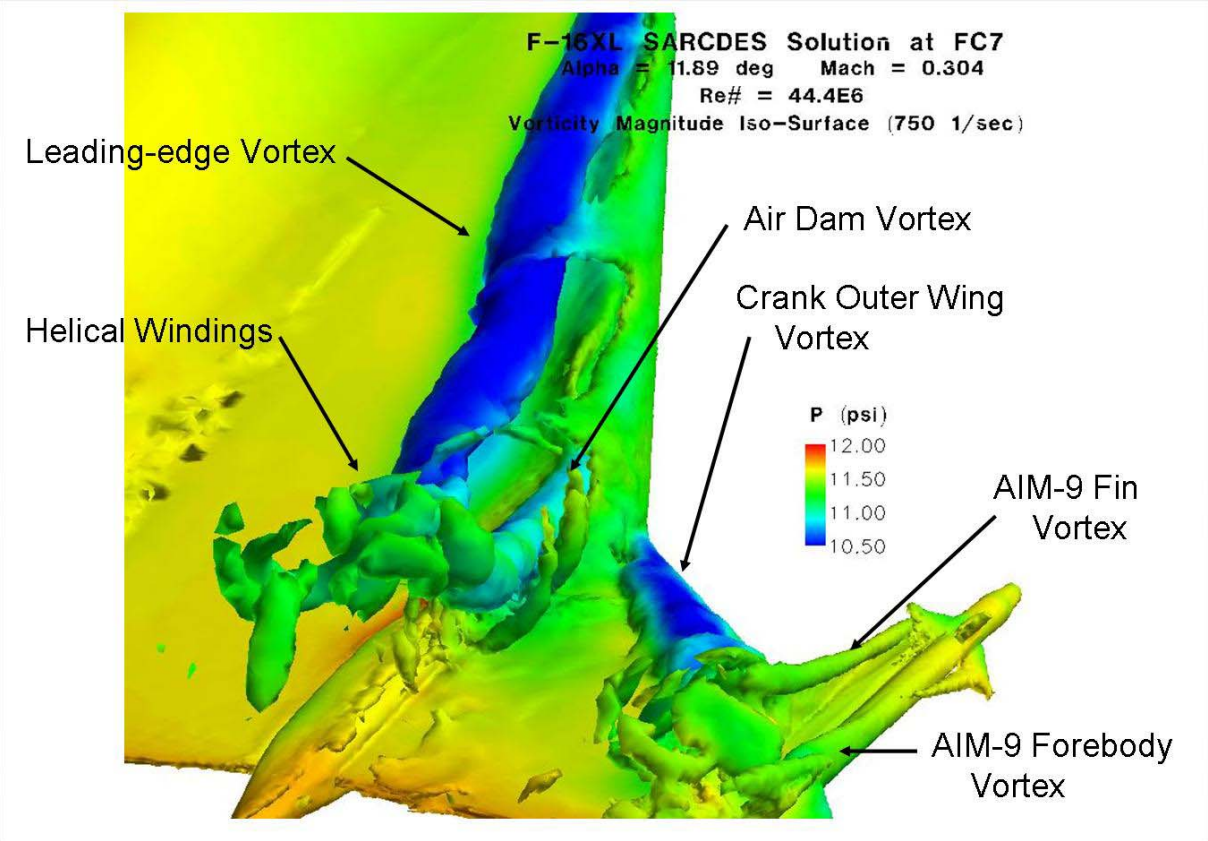

Figure 9-10: Close Up View of the Vortical Flowfield above the F-16XL-1 at Flight Condition 7; Iso-Surfaces of Vorticity Magnitude Colored by Pressure at an Instant in Time.

Determining the time-accurate characteristics of the flowfield is the central theme of this paper and so it becomes important to determine the relationship between the instantaneous solution, time-averaged solution, and a steady RANS solution. Figure 9-11 depicts iso-surfaces of vorticity magnitude and C_p at an instant in time on the lower half of the figure and a time average after 2000 time steps on the top half of the figure. The "pre-breakdown like" regions of each of the vortices seem comparable in position, size, and strength of both the vortices and their corresponding pressure "foot-prints" on the surface for the time averaged and instantaneous solutions. Aft of the breakdown-like region the helical windings are averaged out into a coherent structure. The time averaged solution is also very similar to the steady RANS solution using the SARC turbulence model (see Figure 9-12), although there are some differences aft of the breakdown-like region. Many of the standard turbulence models are unable to capture the post-breakdown windings as accurately as the SARC model [[9-5][9-6][9-8][9-9][9-10]].

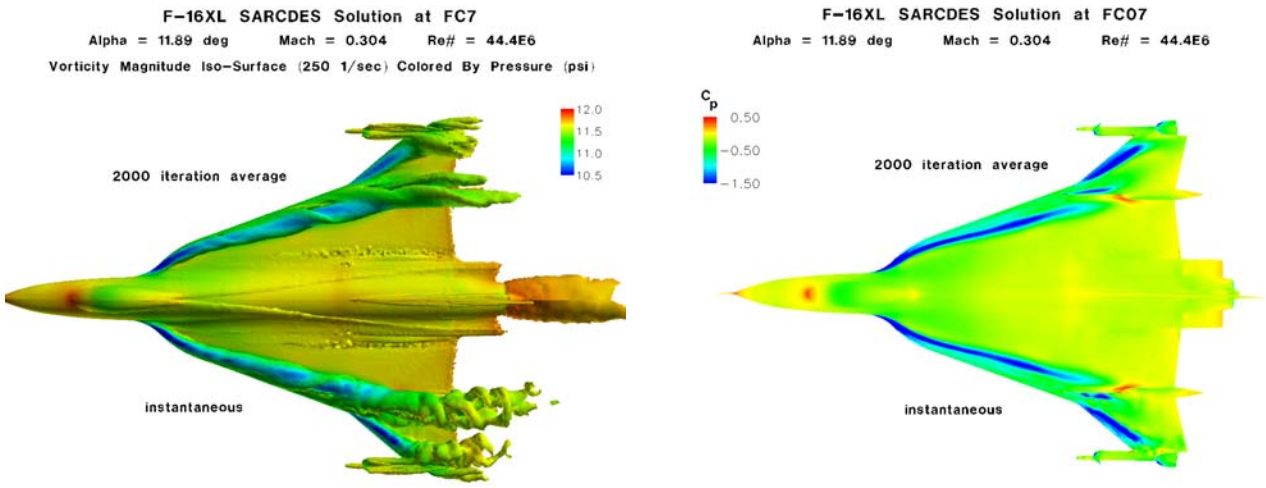

(a) (b)

Figure 9-11: Comparison of an Instantaneous Solution to a Solution Time-Averaged after 2000 Time Steps: (a) Iso-Surfaces of Vorticity Magnitude Colored by Pressure; (b) Surface Pressure Coefficient Distribution, C_p.

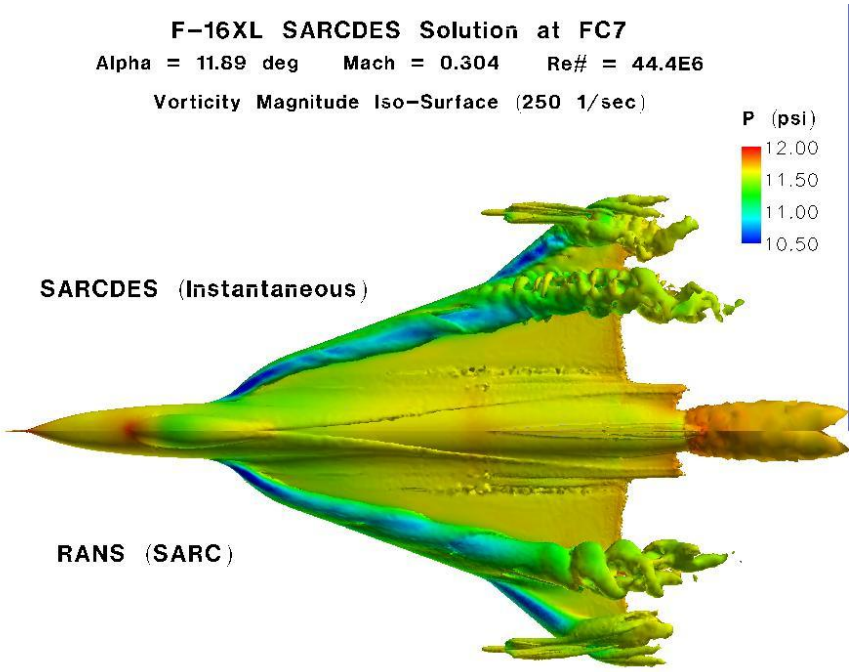

Figure 9-12: Comparison of an Instantaneous SARCDES Solution (upper half) to a SARC RANS Solution (lower half); Iso-Surfaces of Vorticity Magnitude Colored by Pressure.

Figure 9-13 depicts cross-planes of x-vorticity for various FS locations for both time averaged (left half of each pane) and instantaneous solutions (right half of each pane). At FS300 the shear layer emanating from the

wing leading-edge and the resulting vortex core can be seen in red and the secondary vortex can be seen below the primary vortex in blue. FS300 through FS375 all show similar vortical structures and very little difference between the time averaged and instantaneous solutions. At FS407.5 the air dam is just visible and the resulting vortex from the air dam has become apparent (in blue) as well as its effect on the secondary vortex previously seen. At FS450 the air dam vortex has lifted off the surface and begun to pair with the leading-edge vortex. The crank outer-wing vortex is also evident in red as well as the AIM-9 fin vortices (blue and red) at FS450. There are only minor differences in the time averaged versus instantaneous solutions evident in FS407.5 and FS450. At FS492.5 the same features exist but a large difference between the time averaged and instantaneous solutions can be observed due to the breakdown and resulting helical windings of the primary, outer crank, and AIM-9 fin vortices.

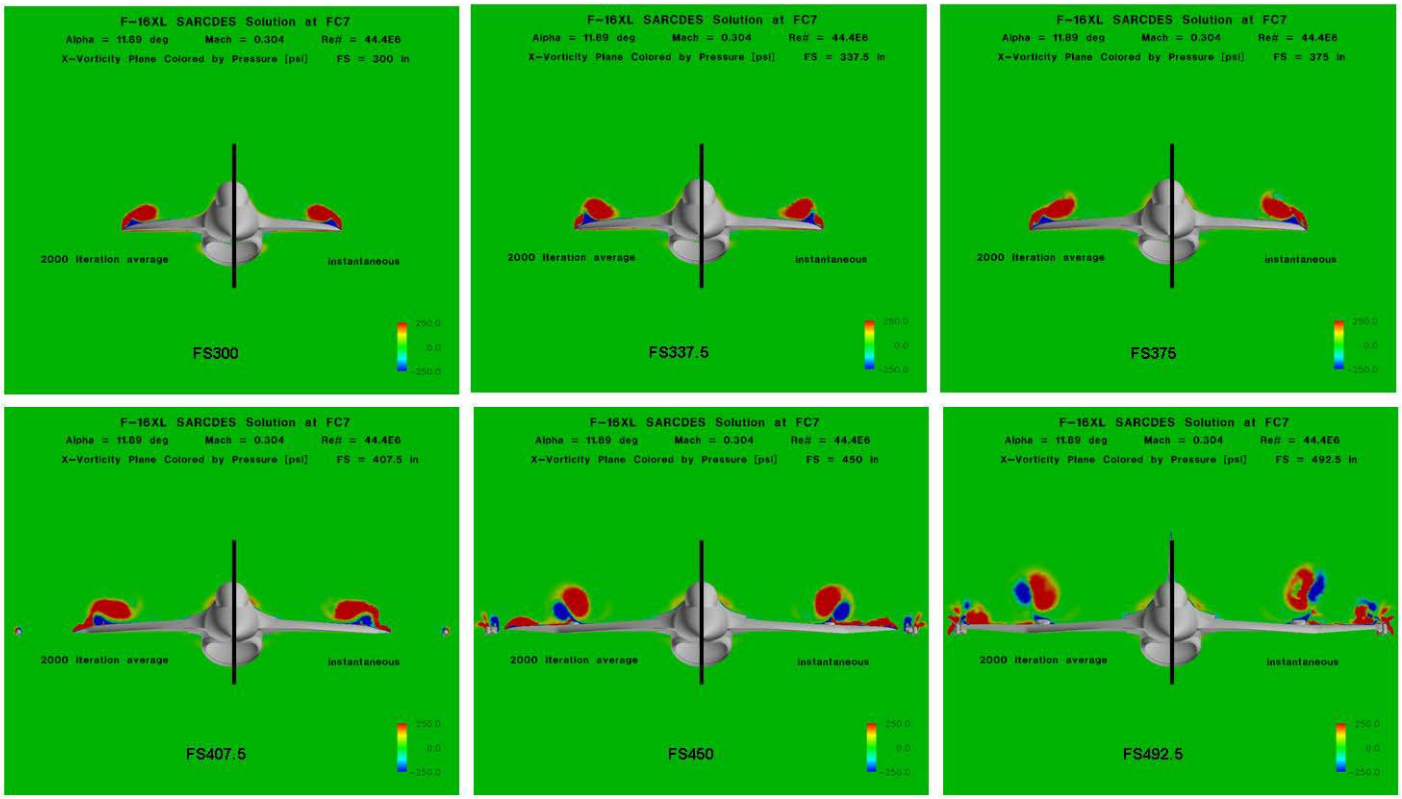

Figure 9-13: Flight Condition 7; Cross-Planes of Vorticity in the x-Coordinate Direction (Down the Fuselage Axis).

Up to this point all of the data has been computational to show the complex flow features evident at this flight condition. Figure 9-14 depicts the flight test surface pressure coefficient, C_p, data compared to the computed time averaged C_p, computed min and max C_p at a given location, and the related RANS solution C_p for FC7 at various BL positions. As discussed earlier, the flight test data is at a slightly different condition but considered comparable. As is evident in the cross-planes of vorticity away from the air dam or crank, the BL40 through BL95 plots show that unsteady effects are minimal. BL55, BL70, BL80, and BL95 all show good agreement with the available flight test data with only minor discrepancies near the recovery from the strong suction peak. The suction peak C_p value and the position of the peak are in good agreement for all of these BL

locations. BL105 is located just inboard of the air dam/actuator pod and a small amount of unsteadiness is observed as evidenced by a widening of the min C_p, and max C_p curves from the mean C_p and RANS C_p curves. At BL127.5, BL153.5, and BL184.5 there are large differences in the min C_p and max C_p from the mean C_p curves, especially near the vortex induced suction peak, although the mean C_p curve compares well with the flight test data. At BL127.5 and BL184.5 we begin to see the difference between the mean C_p computed from a time accurate solution and the RANS C_p. This is especially evident at BL184.5 in the range of x/c from 0.1 to 0.4. In this region there is a large "hump" with the time-averaged C_p showing the best agreement with flight test. This discrepancy has been observed in other fighter aircraft simulations and is typically due to the inability of the RANS turbulence models to accurately capture the effect of the massive separation and strong unsteady vortices [[9-5][9-6][9-8][9-9][9-10]].

Figure 9-15 depicts similar data for various FS positions for FC7. As is true of all BL positions, all FS positions are in excellent agreement with the available flight test data. It is also evident at FS407.5, FS450, and FS492.5 that there is significant unsteadiness outboard of the air dam/actuator pod. This unsteadiness is due to the vortices from the air dam/actuator pod, crank outer wing, and AIM-9 tip missile and results in large variations in C_p in this region.

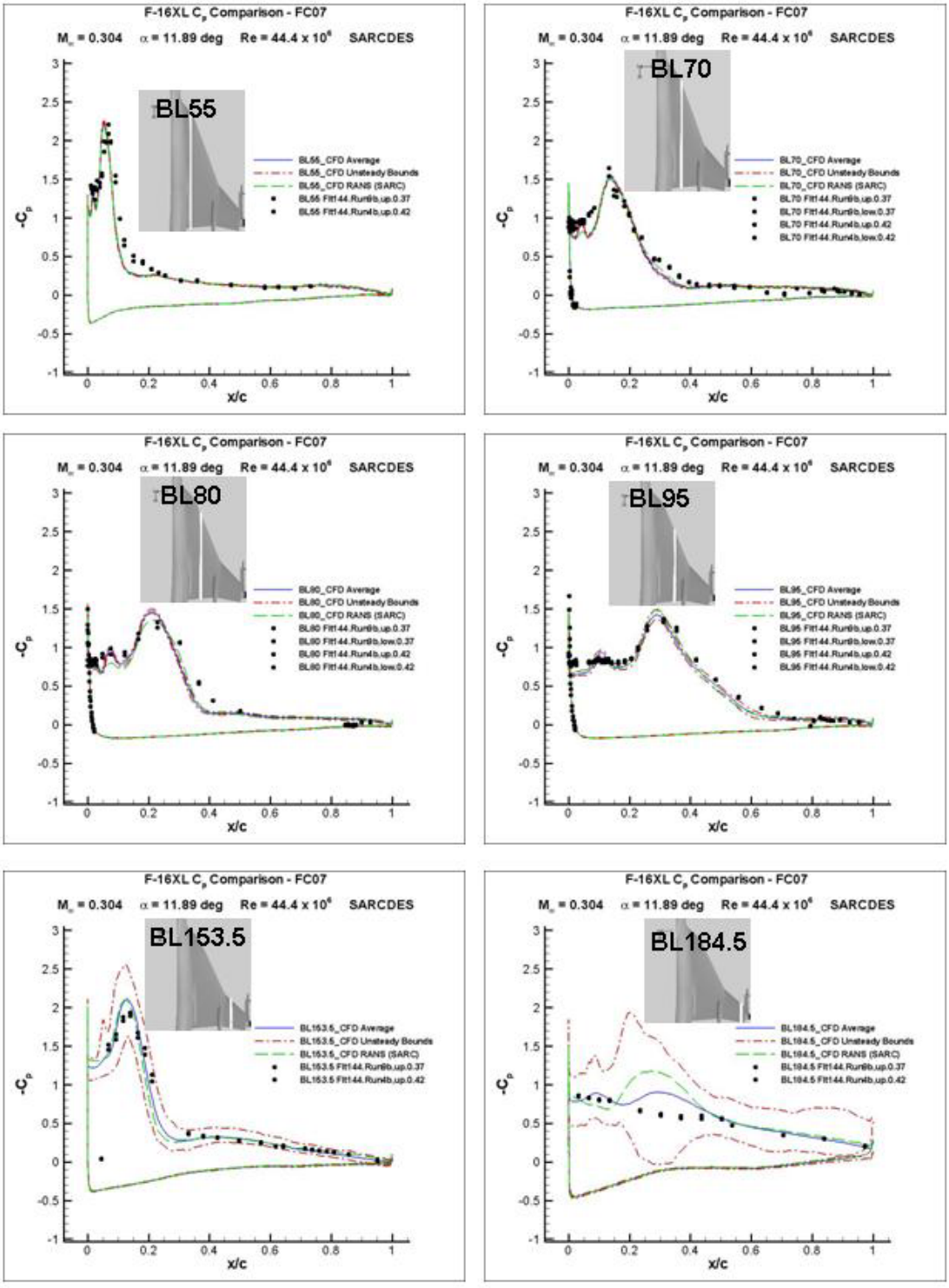

Figure 9-14: Flight Condition 7; Surface C_p along Various F-16XL Butt Line Stations (BL) for Flight Test, Computed Mean, and Computed Max and Min Value for a Series of Time Accurate Solutions.

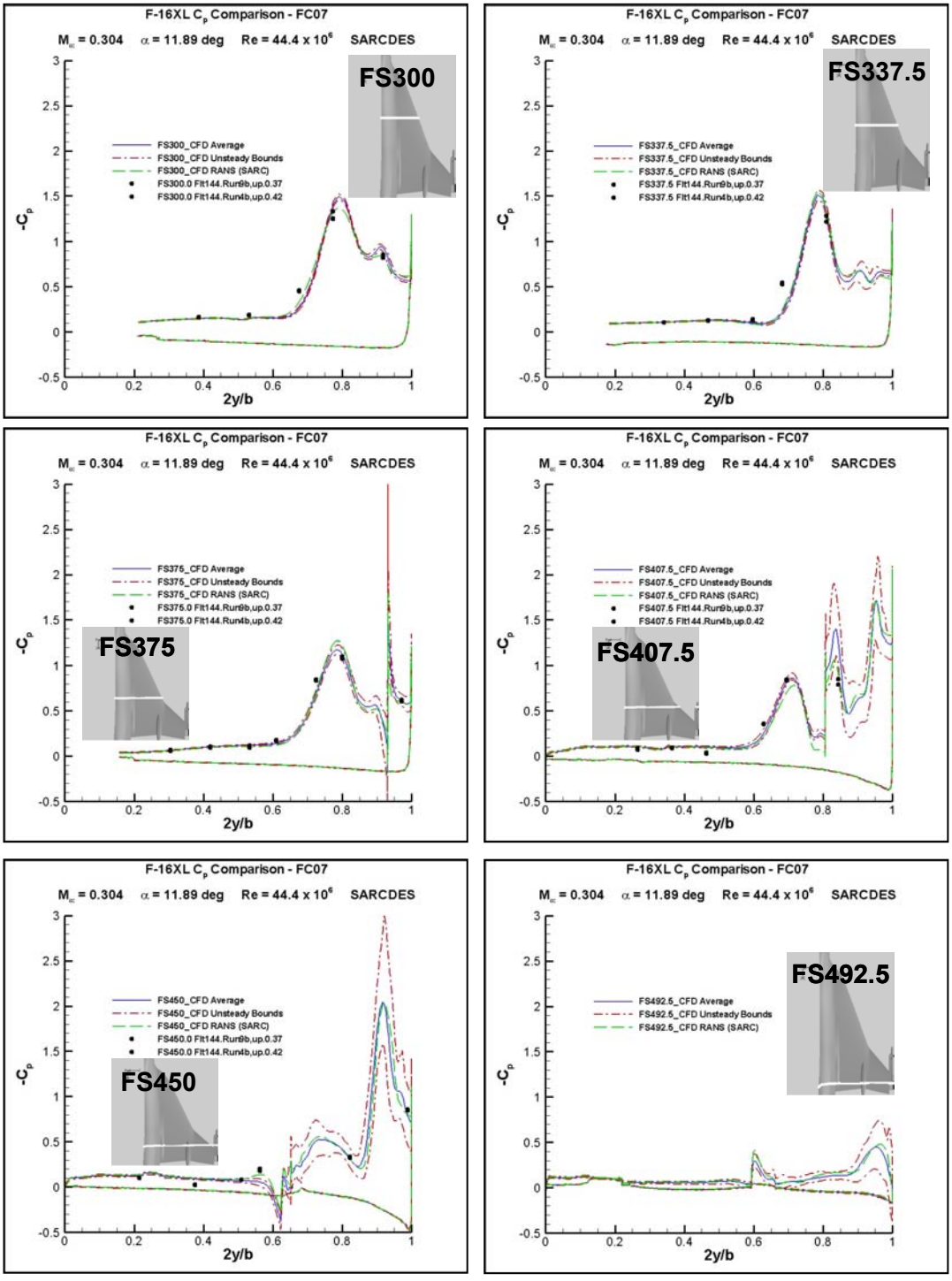

Figure 9-15: Flight Condition 7; Surface C_p along Various F-16XL Fuselage Stations (FS) for Flight Test, Computed Mean, and Computed Max and Min Values.

Figure 9-16 depicts the boundary layer rake comparisons between flight test and computed time average, min, and max scaled velocities at four locations in the neighborhood of FS300. The rakes are at locations along a line approximately perpendicular to the leading edge with Rake 3 most inboard and Rake 7 very near the leading edge and Rake 4 and Rake 5 in between. Rake 3 is well inboard of the leading edge vortex and shows the best agreement with fight test and essentially no unsteady effects of the vortex. Rake 4 is still in good agreement with the flight test data and we see unsteadiness as measured by the difference between min and max scaled velocity and the mean scaled velocity. In the Rake 5 data we see a large difference in the data near the "knee" in the curve and an increase in the unsteadiness of the data. Rake 7 shows the largest discrepancy from flight test including a velocity at the knee higher than the rake edge velocity which is not observed in the flight-test data. It should also be noted that this rake experiences a significant amount of unsteadiness. Rake 7 is located in the most challenging flow region due to the separation occurring somewhere near the leading edge and the transition of the model from RANS to LES. This particular data needs further study to determine the cause of the discrepancy.

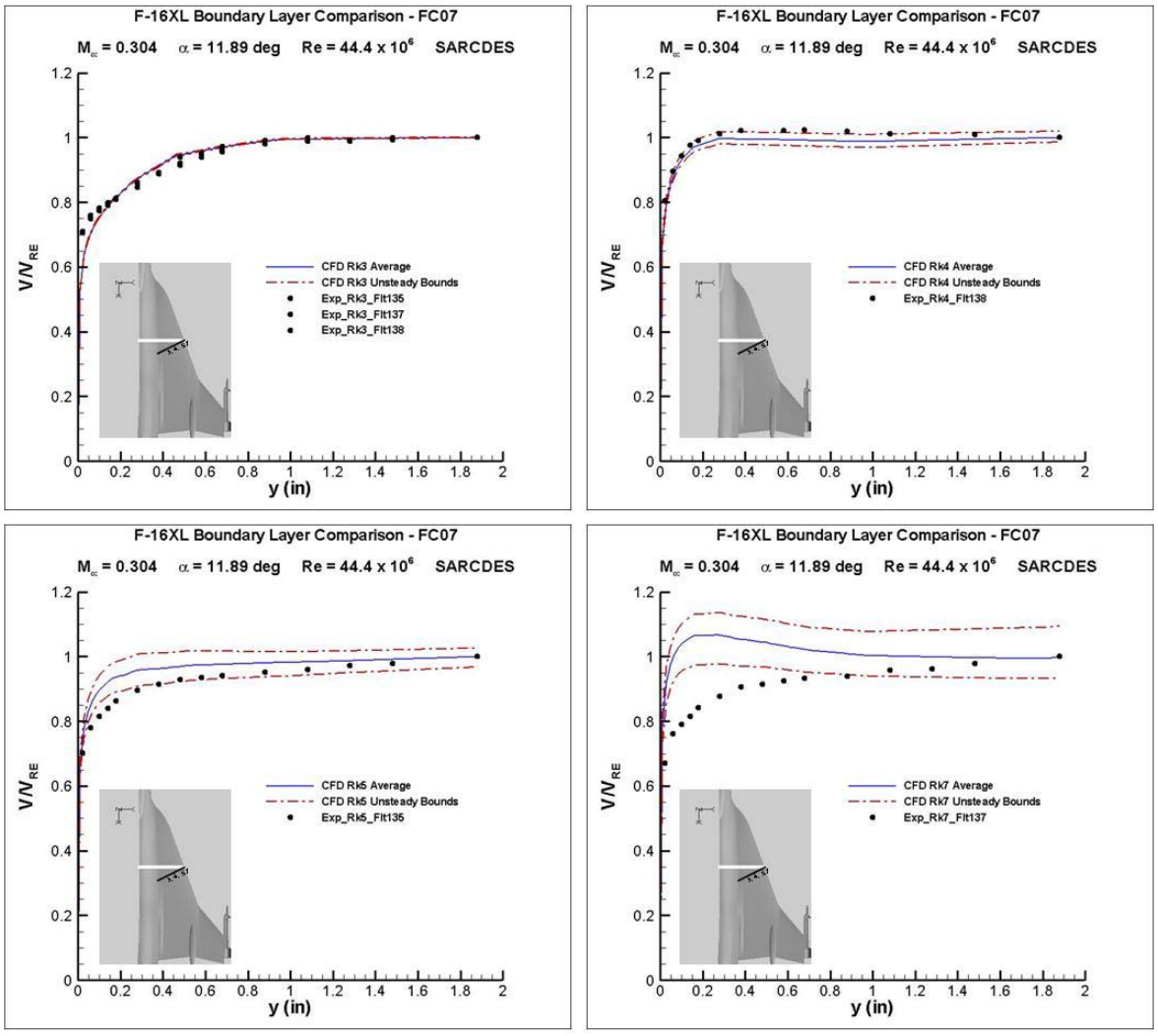

Figure 9-16: Boundary Layer Rake Velocities Scaled by Rake-Edge Velocity for Rakes 3, 4, 5, and 7 at Flight Condition 7.

9.4.2.2 Flight Condition 19

Flight Condition 19 (FC19) is at an angle of attack of 11.85 degrees, a Mach number of 0.36, and an altitude of 10,000 ft resulting in a Reynolds number of 46.8 million. This condition was chosen for comparison due to the availability of skin friction data. Figure 9-17 depicts the flowfield over the F-16XL at FC19. As in FC7, iso-surfaces of vorticity magnitude of 250 1/sec colored by pressure are shown in the perspective view and surface C_p for the right wing are shown in the planform view. The dominant features of the flowfield are the same as in FC7 with only slight differences.

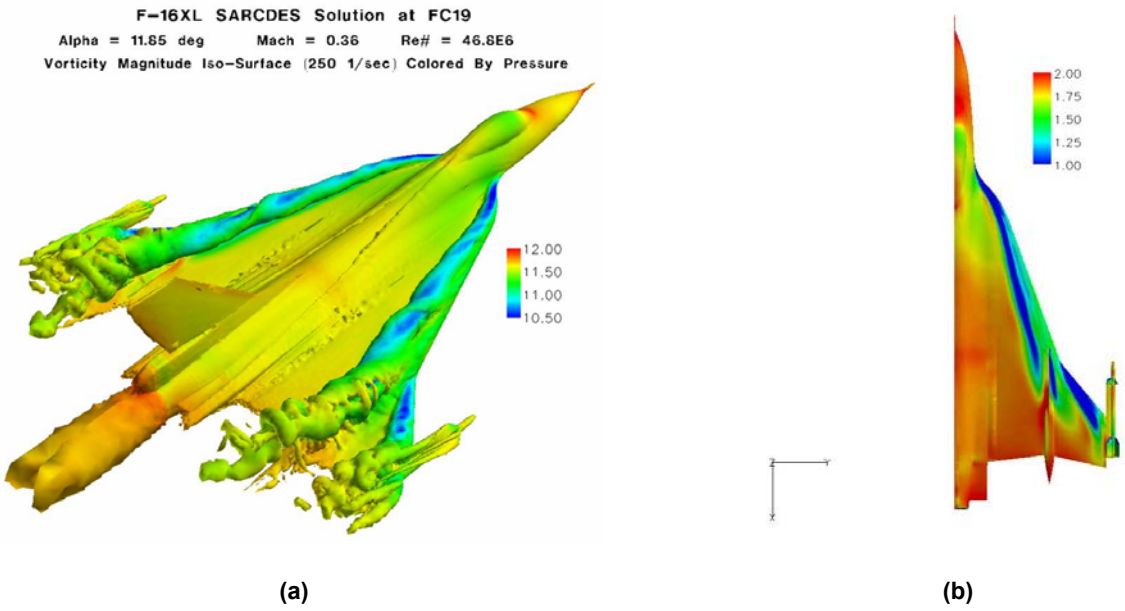

Figure 9-17: Flight Condition 19: (a) Iso-Surfaces of Vorticity Magnitude Colored by Pressure; (b) Surface Pressure Coefficient Distribution, C_p.

Figure 9-18 depicts the local skin friction coefficient along FS330 for flight test and computed mean, min, and max. The flight test and computed data compare well qualitatively with the shape and position of the primary peak. However, quantitatively the magnitude of the skin friction coefficient primary peak is 22% different than the flight test data. It is well known that skin friction is one of the more challenging coefficients to match and may need additional grid resolution to improve the flight test data comparison. The secondary peak is well within the min and max values of the skin friction coefficient.

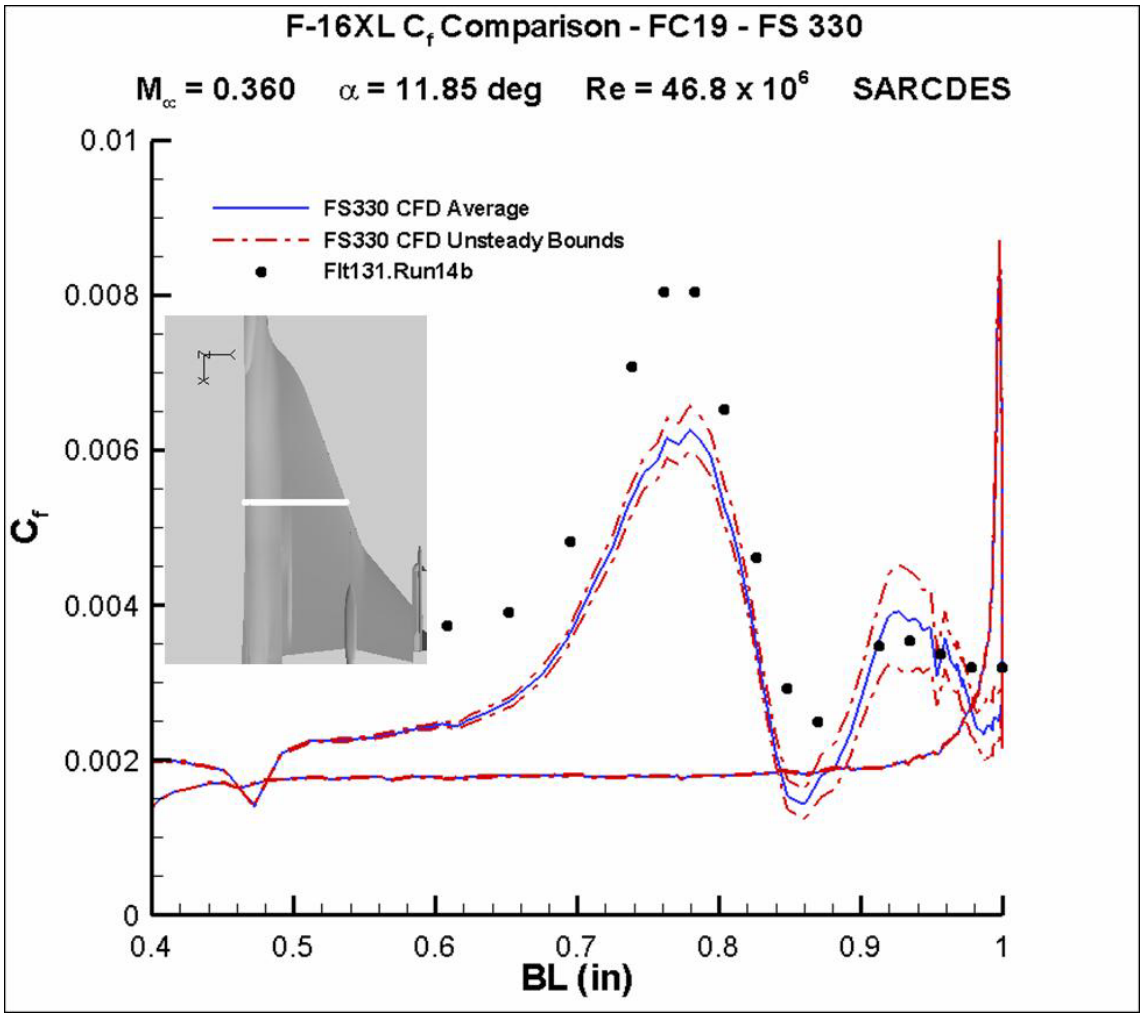

Figure 9-18: Local Skin Friction Coefficient along Fuselage Station 330.

9.4.2.3 Flight Condition 46

Flight Condition 46 (FC46) is at an angle of attack of 10.4 degrees, a Mach number of 0.527, and an altitude of 24,000 ft resulting in a Reynolds number of 46.9 million. This condition was chosen for comparison due to the availability of skin friction data. Figure 9-19 depicts the flowfield over the F-16XL at FC46. As in FC7, iso-surfaces of vorticity magnitude of 250 1/sec colored by pressure are shown in the perspective view and surface C_p for the right wing are shown in the planform view. The dominant features of the flowfield are the same as in FC7 with only slight differences.

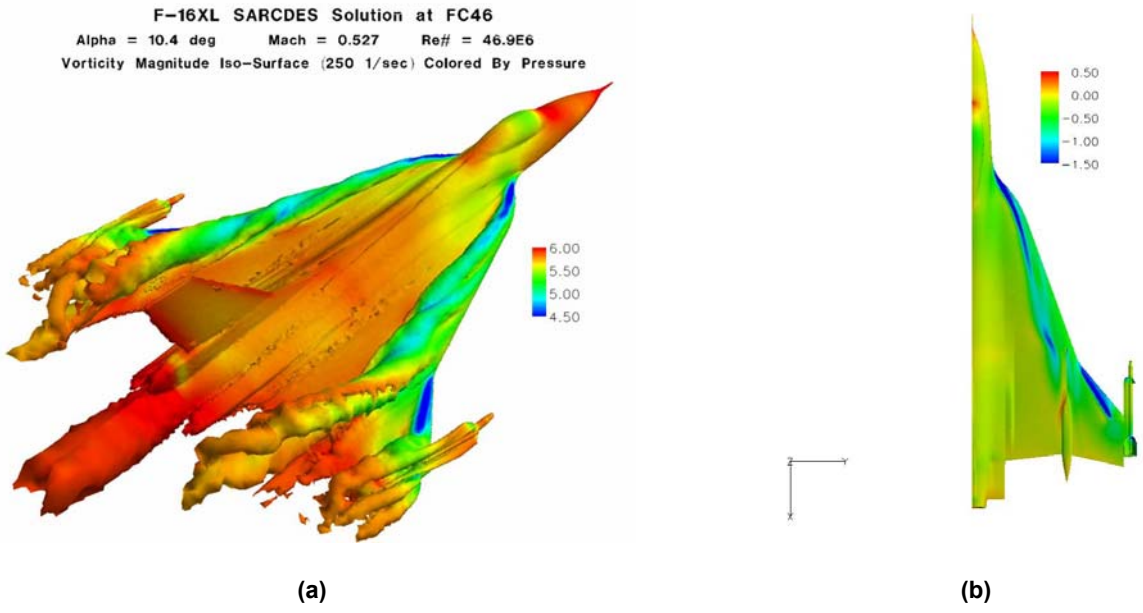

Figure 9-19: Flight Condition 46: (a) Iso-Surfaces of Vorticity Magnitude Colored by Pressure; (b) Surface Pressure Coefficient Distribution, C_p.

Figure 9-20 depicts the flight test C_p data compared to the computed time averaged C_p, and computed min and max C_p at a given location for FC46 at various BL positions. As is the case with FC7, the BL40 through BL70 plots show that unsteady effects are minimal. However unlike FC7, FC46 shows unsteadiness in BL80 and BL95. The flight test comparison for BL55 is in excellent agreement in both shape and magnitude of surface C_p. Both BL70 and BL80 are in good agreement as well, with a slight shift outboard in the suction peak position and a slightly higher over all magnitude for the computational data. At BL95 the computations over predict the magnitude of both the primary and secondary vortex and predict a much sharper primary vortex. The BL153.5 computational data show an over prediction in suction peak magnitude and a shift outboard in the peak location. The BL184.5 computational data shows significant unsteadiness as in the FC7 case with the majority of the data within the min and max C_p bounds of the computational data. However, the computational data misses the inboard trend of a higher C_p. Overall this can be considered a fairly good comparison with flight test but due to the excellent agreement between flight test and computations for FC7, it is possible the actual flight test for FC46 may have been at a slightly different condition than simulated.

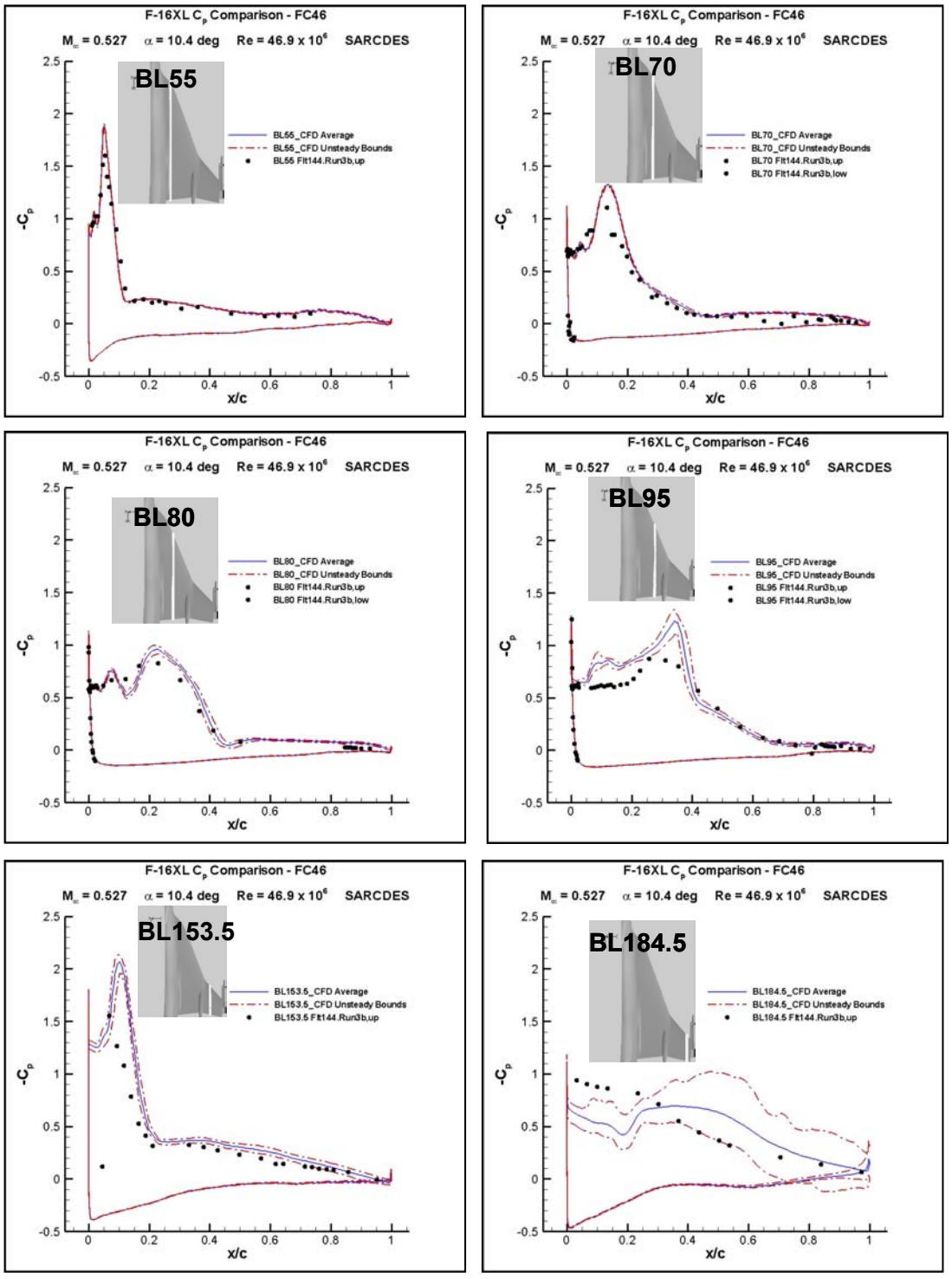

Figure 9-20: Flight Condition 46: Surface C_p along Various F-16XL Butt Line Stations (BL) for Flight Test, Computed Mean, and Computed Max and Min Value for a Series of Time Accurate Solutions.

9.4.2.4 Flight Condition 25

Flight Condition 25 (FC25) is at an angle of attack of 19.84 degrees, a Mach number of 0.242, and an altitude of 10,000 ft resulting in a Reynolds number of 32.2 million. This condition was added by the CAWAPI RTO Task Group to give a high angle of attack comparison case. Figure 9-21 depicts the flowfield over the F-16XL at FC25. Iso-surfaces of vorticity magnitude of 250 1/sec colored by pressure are shown in the perspective view and surface C_p for the right wing are shown in the planform view. As in the case of FC7, it is apparent that the dominant features of the flowfield are the leading-edge vortex, the air-dam vortex, the outer-wing vortex, and a complicated set of vortices from the AIM-9 fins and fore-body. However, the increased angle of attack has caused the breakdown of these vortices to occur earlier creating a more significantly unsteady flowfield. It is easier to label this classic vortex breakdown due to the fact that the breakdown position is well forward and inboard of the air dam/actuator pod. Figure 9-22 shows a close up view of this region for an iso-surface of vorticity-magnitude level of 900 1/sec with labels for the dominant features. The approximate breakdown position of the leading-edge vortex is FSXXX and the crank outer wing vortex is FSXXX.

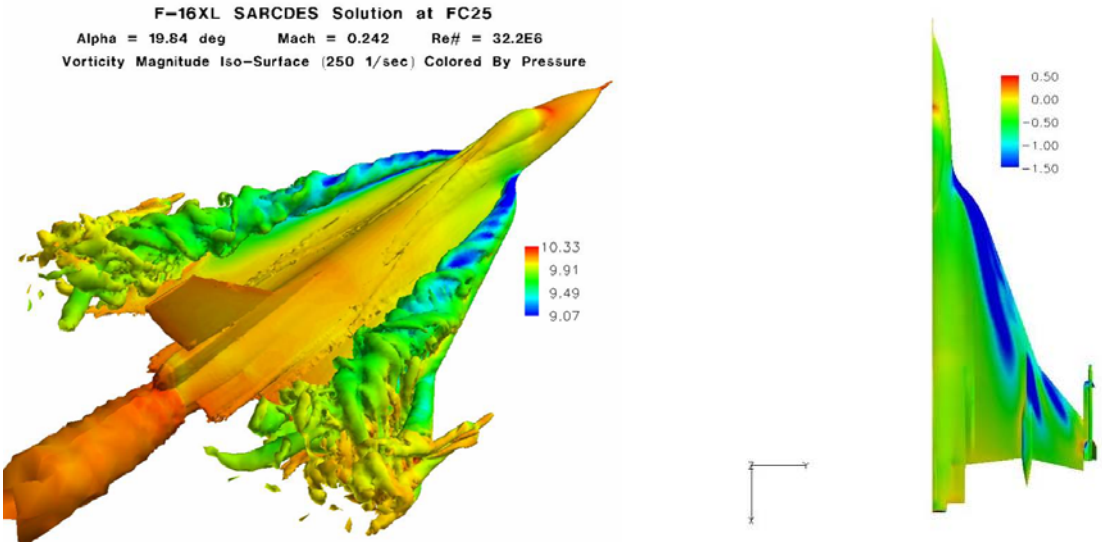

(a) (b)

Figure 9-21: Flight condition 25: (a) Iso-Surfaces of Vorticity Magnitude Colored by Pressure; (b) Surface Pressure Coefficient Distribution, C_p.

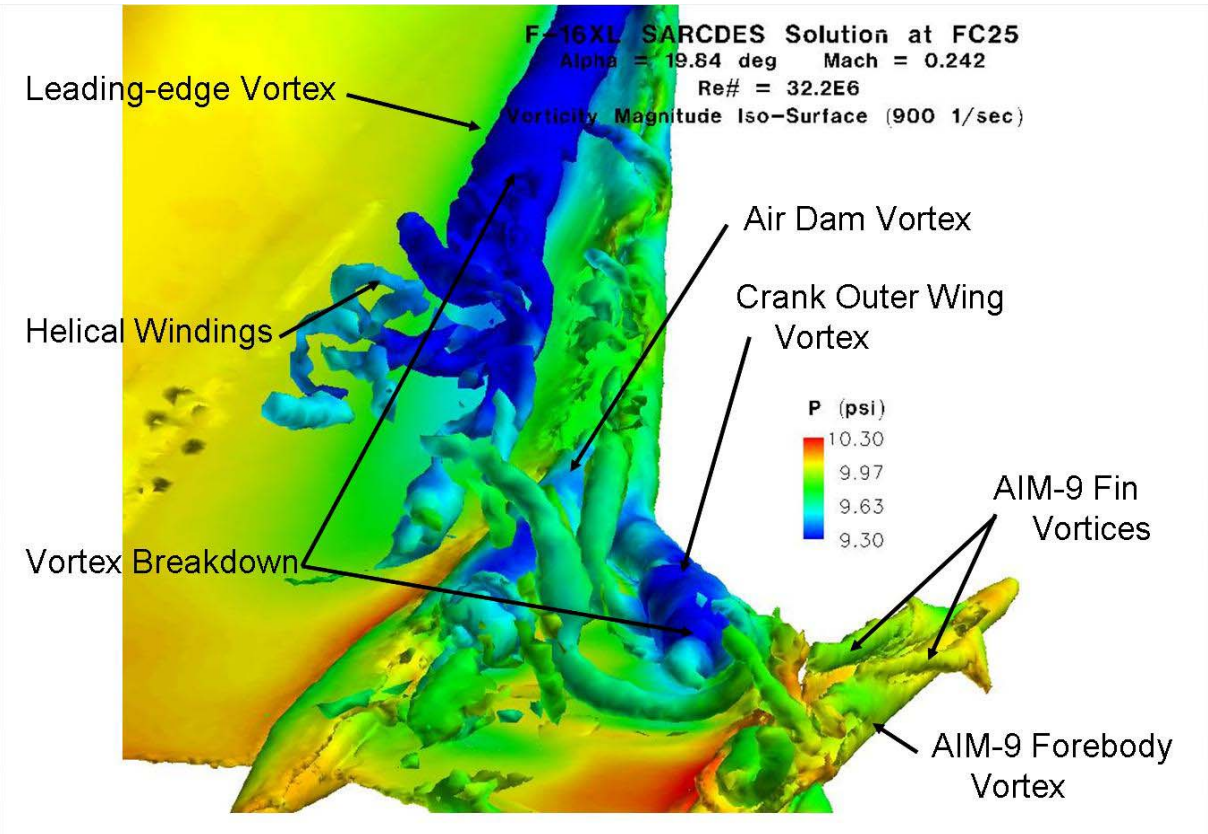

Figure 9-22: Close Up View of the Vortical Flowfield above the F-16XL-1 at Flight Condition 25; Iso-Surfaces of Vorticity Magnitude Colored by Pressure.

Figure 9-23 depicts the flight test C_p data compared to the computed time averaged C_p, and computed min and max C_p at a given location for FC25 at various BL positions. The BL40 through BL70 plots show that unsteady effects are minimal. The BL80, BL95, and BL105 positions all show measurable unsteadiness. BL55, BL70, BL80, and BL95 all show excellent agreement with flight test data for this condition. The BL127.5, BL153.5, and BL184.5 positions all show significant unsteadiness in the surface C_p. All of the flight test data is within the bounds of the computed C_p min and max curves. Overall, there is excellent agreement with the flight test data for this flight condition and the comparison shows the utility of hybrid turbulence models and reliable CFD solvers to compute these complex unsteady fighter flowfields.

Figure 9-24 depicts similar data for various FS positions at FC25. As is true of all BL positions, all FS positions are in excellent agreement with the available flight test data. It is also evident that there is significant unsteadiness on the F-16XL wing at all FS positions aft of FS300 at this flight condition.

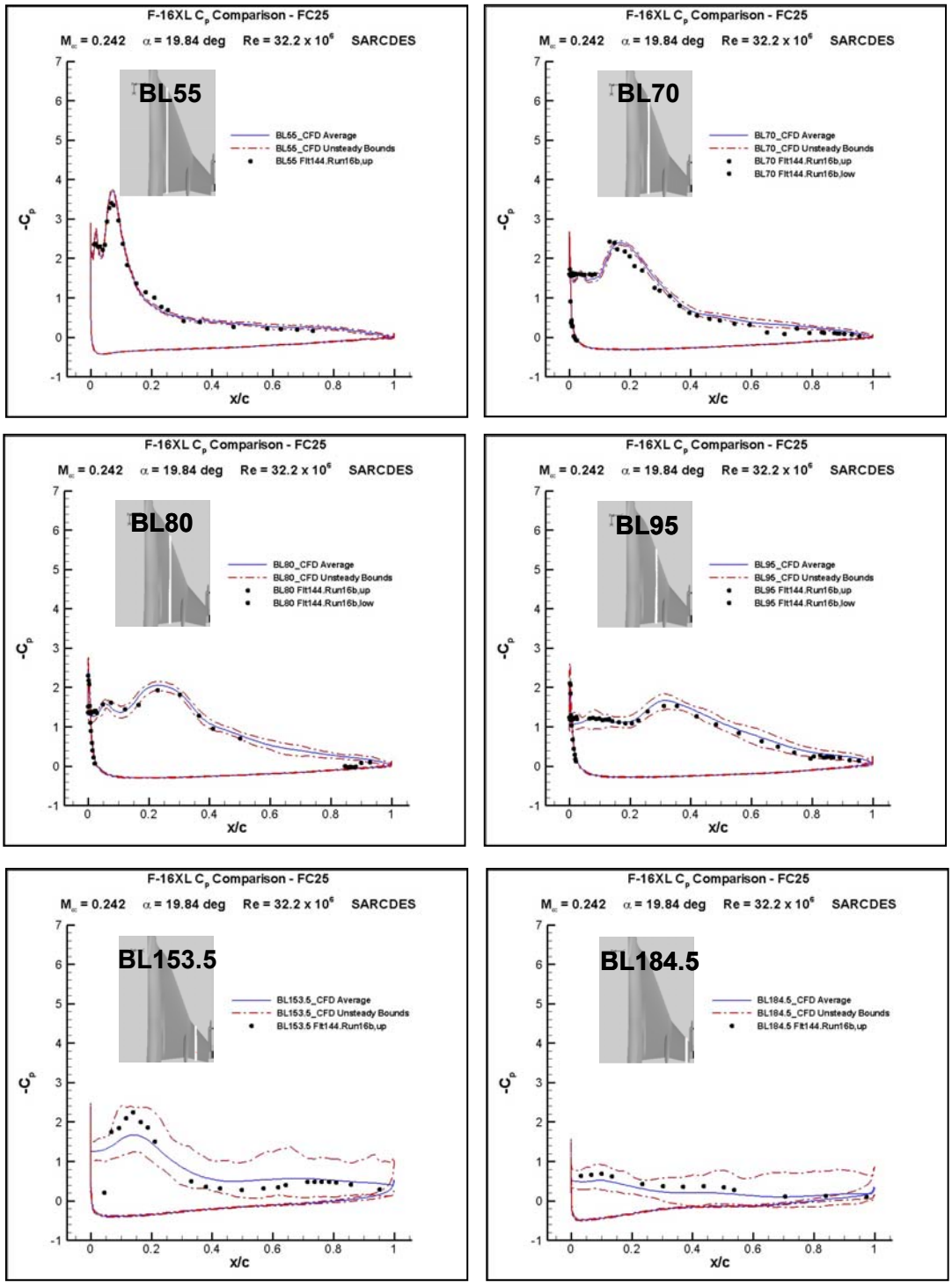

Figure 9-23: Flight Condition 25: Surface C_p along Various F-16XL Butt Line Stations (BL) for Flight Test, Computed Mean, and Computed Max and Min Value for a Series of Time Accurate Solutions.

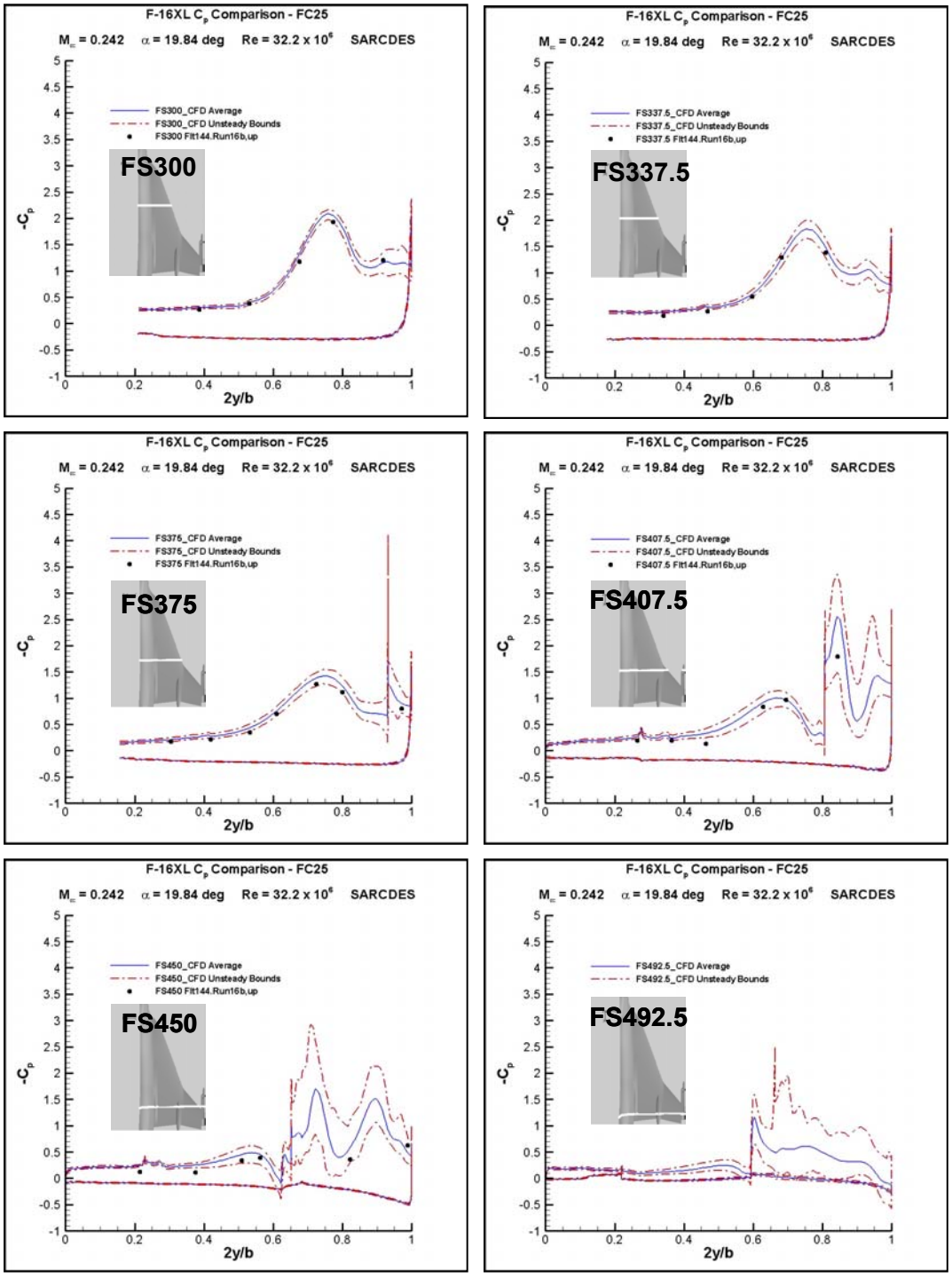

Figure 9-24: Flight Condition 25: Surface C_p along Various F-16XL Fuselage Stations (FS) for Flight Test, Computed Mean, and Computed Max and Min Values.

9.4.3 Transonic Flight Condition 70 (FC70)

The only transonic condition chosen by the CAWAPI RTO Task Group is Flight Condition 70. FC70 is at a Mach number of 0.97, an angle of attack of 4.37 degrees, and an altitude of 22,300 ft resulting in a Reynolds number of 88.8 million. Figure 9-25 depicts the flowfield over the F-16XL at FC70. Iso-surfaces of vorticity magnitude of 250 1/sec colored by pressure are shown in the perspective view and surface C_p for the right wing are shown in the planform view. The dominant features for this flowfield are no longer the same as the subsonic cases. There is a leading edge vortical structure that detaches from the leading edge and turns streamwise just after the s-curve portion of the leading edge. Also, the air dam/actuator pod and AIM-9 fin and forebody vortices exists but are minimal and close to the surface. Of course the more important features are the transonic shocks that are evident in the surface C_p distribution. The emphasis of this paper is the unsteady effects, which are essentially non-existent for this flowfield, so the data is provided for completeness but will not be discussed in great detail.

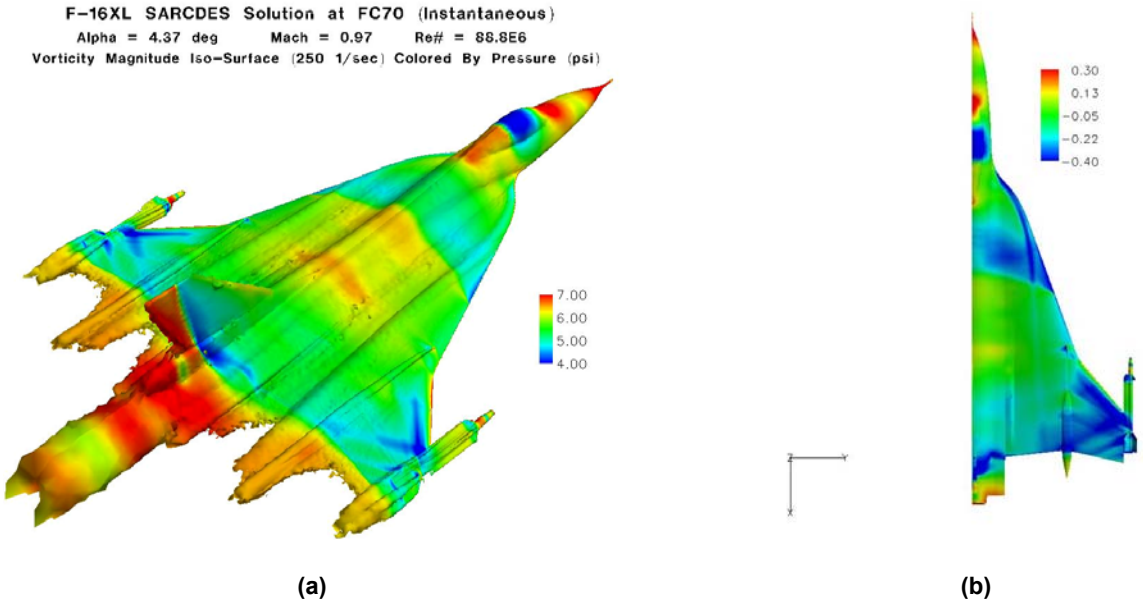

Figure 9-25: Flight Condition 70: (a) Iso-Surfaces of Vorticity Magnitude Colored by Pressure; (b) Surface Pressure Coefficient Distribution, C_p.

Figure 9-26 depicts the flight test C_p data compared to the computed time averaged C_p, and computed min and max C_p at a given location for FC70 at various BL positions. The BL40 through BL184.5 plots show that unsteady effects are minimal. The BL55 and BL95 data are in good agreement with flight test data but the BL70, BL80, BL153.5, and BL184.5 data are in rather poor agreement with flight test data. This poor agreement may be due to the fact that a control surface in the outer portion of the wing was deflected in flight test but not in the grid. This discrepancy was discovered by the CAWAPI RTO Task Group too late in the study to make changes to the grid and therefore all participants have seen similar discrepancies.

Figure 9-27 shows very similar agreement between flight test and computations for all FS positions as the BL positions.

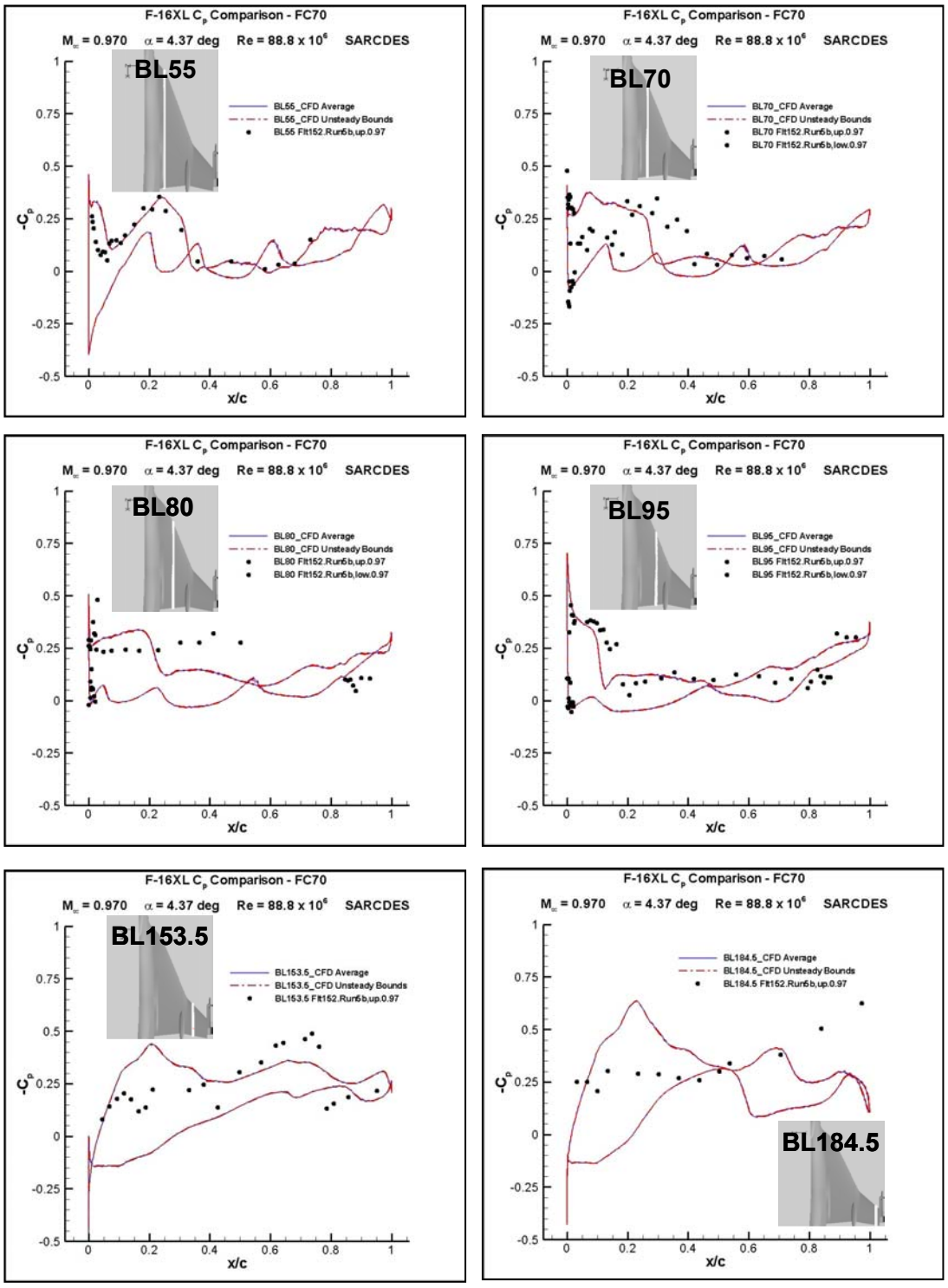

Figure 9-26: Flight Condition 70: Surface C_p along Various F-16XL Butt Line Stations (BL) for Flight Test, Computed Mean, and Computed Max and Min Value for a Series of Time Accurate Solutions.

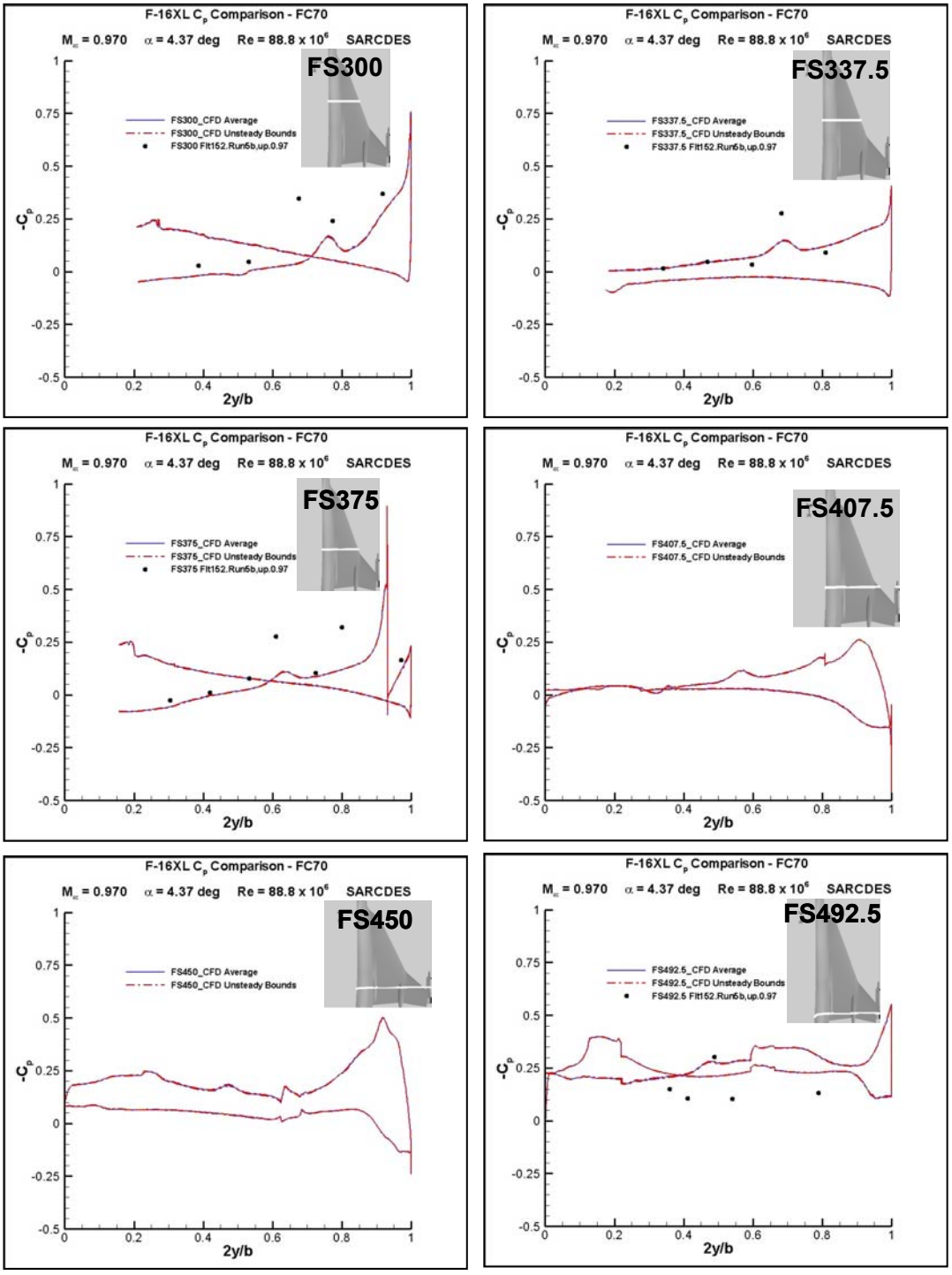

Figure 9-27: Flight Condition 70: Surface C_p along Various F-16XL Fuselage Stations (FS) for Flight Test, Computed Mean, and Computed Max and Min Values.

9.4.4 Sideslip Flight Conditions

There are two flight conditions with non-zero sideslip angles, medium angles of attack, and subsonic Mach numbers. These two conditions have sideslip angles of +5.31 (FC50) and -4.58 (FC51). Solutions were computed for these two conditions with a mirrored full-span grid based on the original half-span grid used in all of the previously discussed computations. This section presents results for these two non-symmetric flight conditions.

9.4.4.1 Flight Condition 50

Flight Condition 50 (FC50) is at a sideslip angle of +5.31 degrees (wind in the right ear), an angle of attack of 13.56 degrees, a Mach number of 0.434, and an altitude of 24,000 ft resulting in a Reynolds number of 39.4 million. Figure 9-28 depicts the flowfield over the F-16XL at FC50. Iso-surfaces of vorticity magnitude of 250 1/sec colored by pressure are shown in the left view and surface C_p is shown in the right view. The dominant features of the left wing are similar to the FC7 baseline case but the right wing has additional vortical structures. The effect of a positive sideslip angle is an increase in the effective angle of attack and a reduction in the leading-edge sweep angle of the right wing. The increased effective angle of attack causes breakdown to occur sooner on the wing and the reduced sweep angle causes the double vortex observed by researchers performing studies of lower sweep delta wings [9-19]. The approximate breakdown position of the leading-edge vortex of the left wing is FSXXX and the right wing is FSXXX.

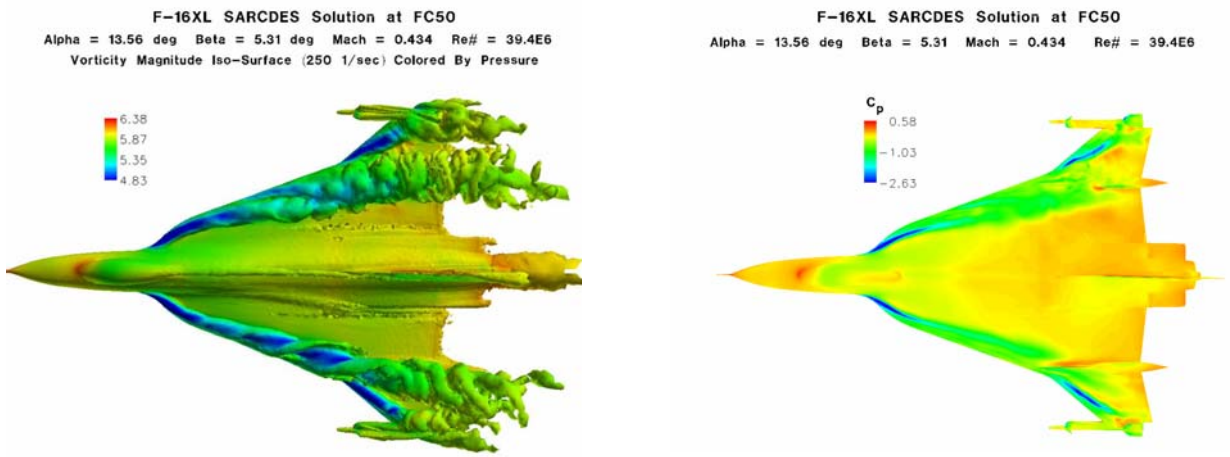

Figure 9-28: Flight Condition 50: (a) Iso-Surfaces of Vorticity Magnitude Colored by Pressure; (b) Surface Pressure Coefficient Distribution, C_p.

Figure 9-29 depicts the right wing flight test C_p data compared to the computed time averaged C_p and computed min and max C_p at a given location for FC50 at various BL positions. It should be noted that for FC50 the comparison data is on the wing with the highest degree of unsteadiness due to the increased effective angle of attack and the reduced leading edge sweep. The BL40 and BL50 plots show that unsteady effects are minimal for these inboard stations and the flight test data matches fairly well for both BL40 and BL55. Unlike FC7, FC19, FC46, or even FC25, FC50 shows significant unsteadiness for BL70 through BL184.5 for the reasons discussed above. The BL70 through BL184.5 flight test data resides primarily inside

of the computed unsteady min and max C_p bounds. However, in BL95 there is a region near the leading edge that is over-predicted by the computations. Overall, these comparisons with flight test are considered good when considering the amount of unsteady massively separated flow on the right wing.

Figure 9-30 depicts similar data for various FS positions for FC50. As is true of all BL positions, all FS positions are in good agreement with the available flight test data and there is significant unsteadiness observed for FS300 through FS492.5 at this flight condition.

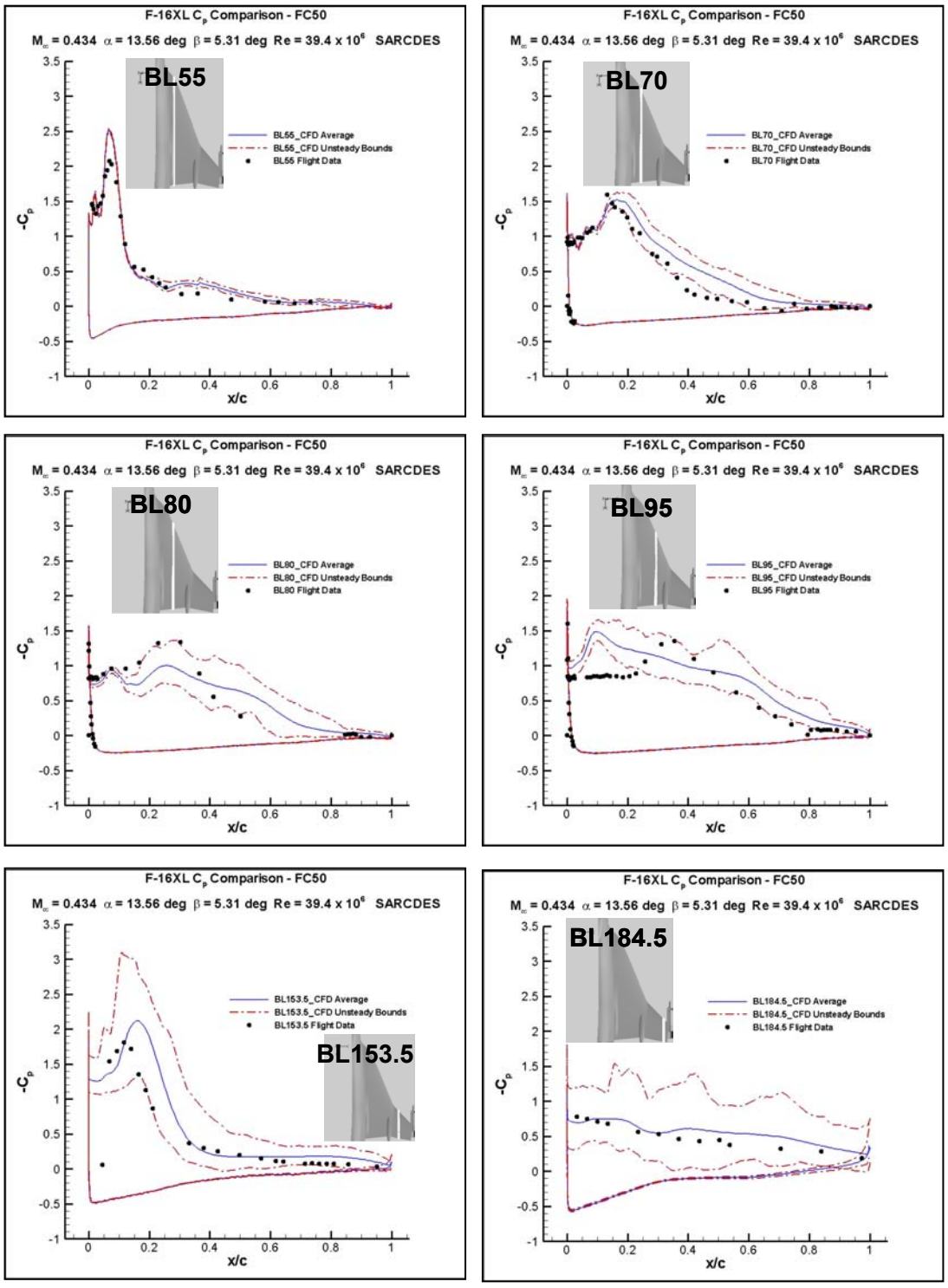

Figure 9-29: Flight Condition 50: Surface C_p along Various F-16XL Butt Line Stations (BL) for Flight Test, Computed Mean, and Computed Max and Min Value for a Series of Time Accurate Solutions.

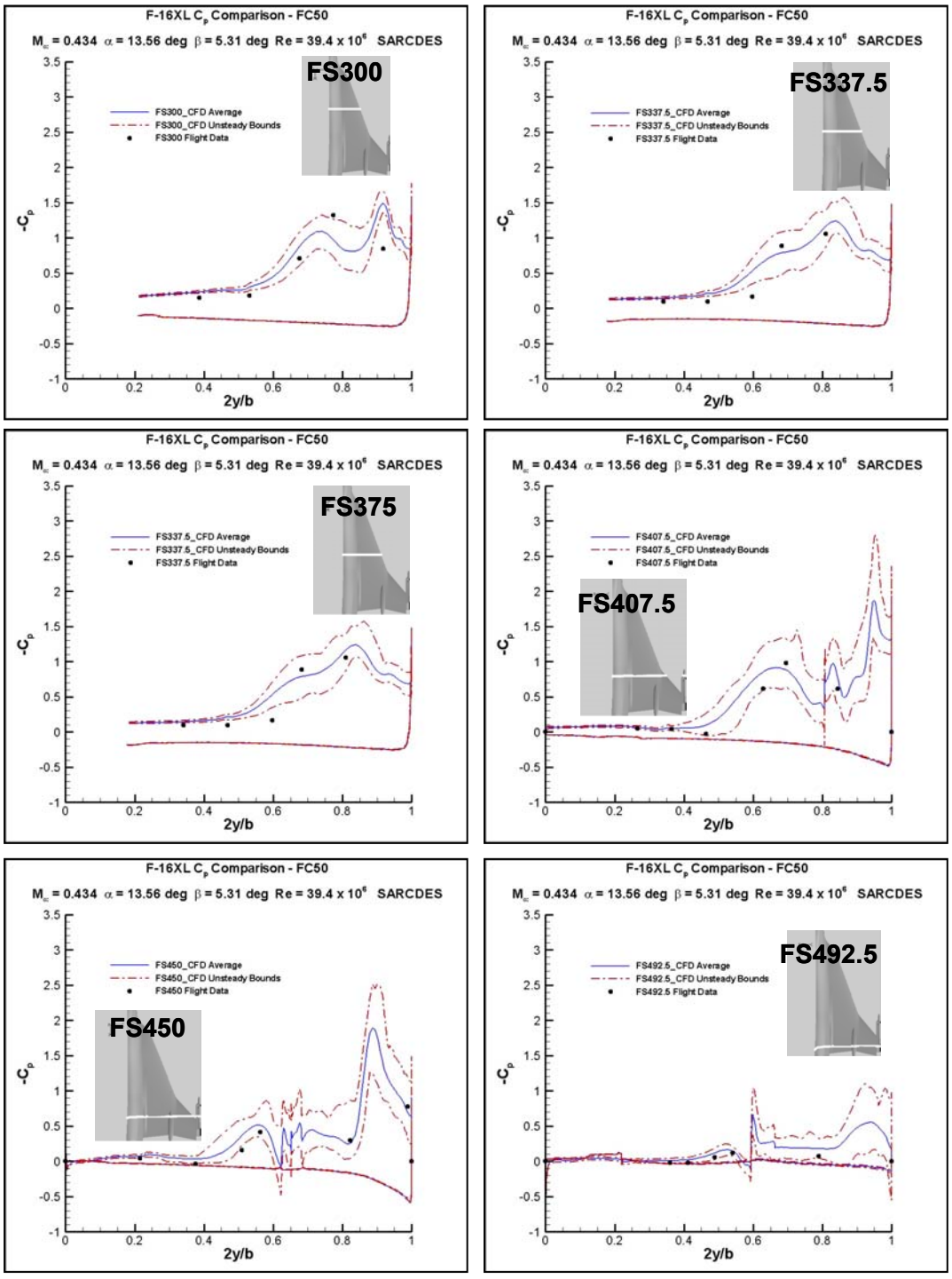

Figure 9-30: Flight Condition 50: Surface C_p along Various F-16XL Fuselage Stations (FS) for Flight Test, Computed Mean, and Computed Max and Min Values.

9.4.4.2 Flight Condition 51

Flight Condition 51 (FC51) is at a sideslip angle of -4.58 degrees (wind in the left ear), an angle of attack of 12.89 degrees, a Mach number of 0.441, and an altitude of 24,000 ft resulting in a Reynolds number of 39.0 million. Figure 9-31 depicts the flowfield over the F-16XL at FC51. Iso-surfaces of vorticity magnitude of 250 1/sec colored by pressure are shown in the left view and surface C_p is shown in the right view. Since the flight conditions of FC51 are nearly the same as FC50 but with an opposite sideslip, the discussions above hold for FC51 but for the opposite wing.

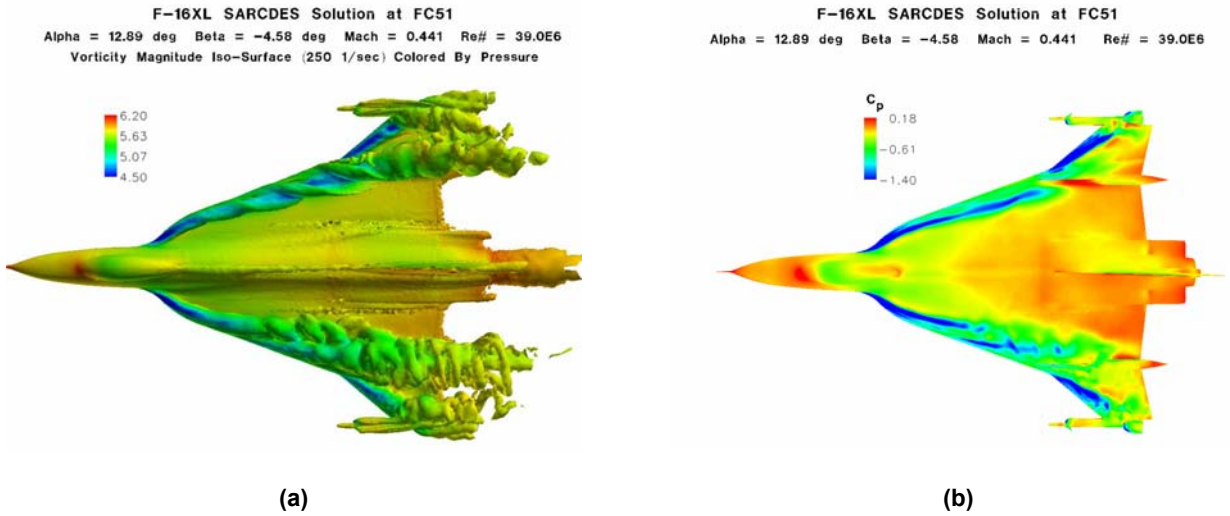

Figure 9-31: Flight Condition 51: (a) Iso-Surfaces of Vorticity Magnitude Colored by Pressure; (b) Surface Pressure Coefficient Distribution, C_p.

Figure 9-32 depicts the right wing flight test C_p data compared to the computed time averaged C_p and computed min and max C_p at a given location for FC51 at various BL positions. It should be noted that for FC51 the comparison data is on the wing with the lowest degree of unsteadiness due to the decreased effective angle of attack and the increased leading edge sweep. The BL40 through BL105 plots show that unsteady effects are minimal and the flight test data matches very well for BL40 through BL105. The BL127.5 plot shows the largest discrepancy with an under-predicted peak located slightly inboard of the flight test data. The BL153.5 and BL184.5 plots show very good agreement with flight test data and a fairly large amount of unsteadiness for BL184.5.

Figure 9-33 depicts similar data for various FS positions for FC51. As is true of all BL positions, all FS positions are in good agreement with the available flight test data and there is very little unsteadiness observed for FS185 through FS492.5 at this flight condition.

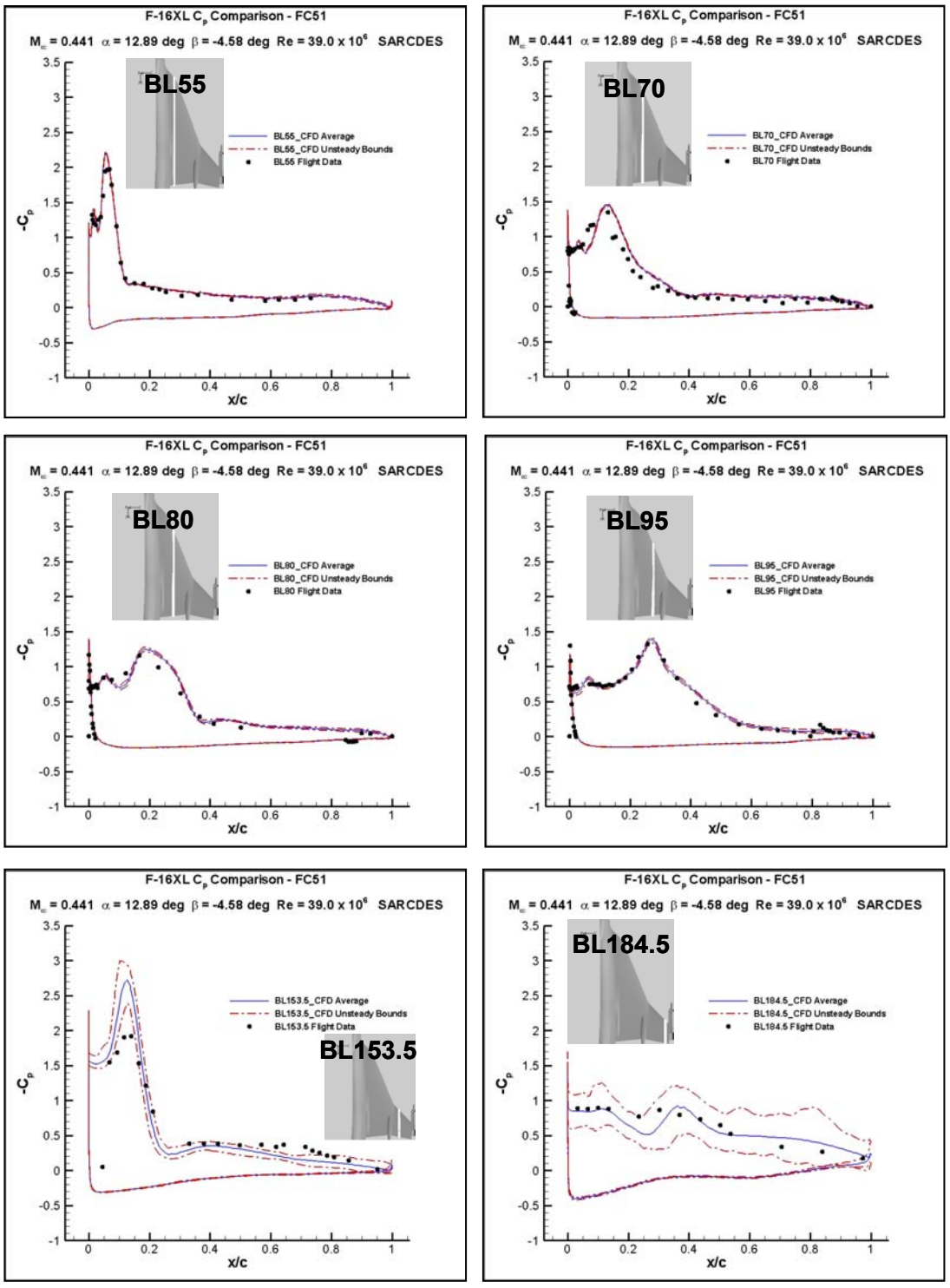

Figure 9-32: Flight Condition 51: Surface C_p along Various F-16XL Butt Line Stations (BL) for Flight Test, Computed Mean, and Computed Max and Min Value for a Series of Time Accurate Solutions.

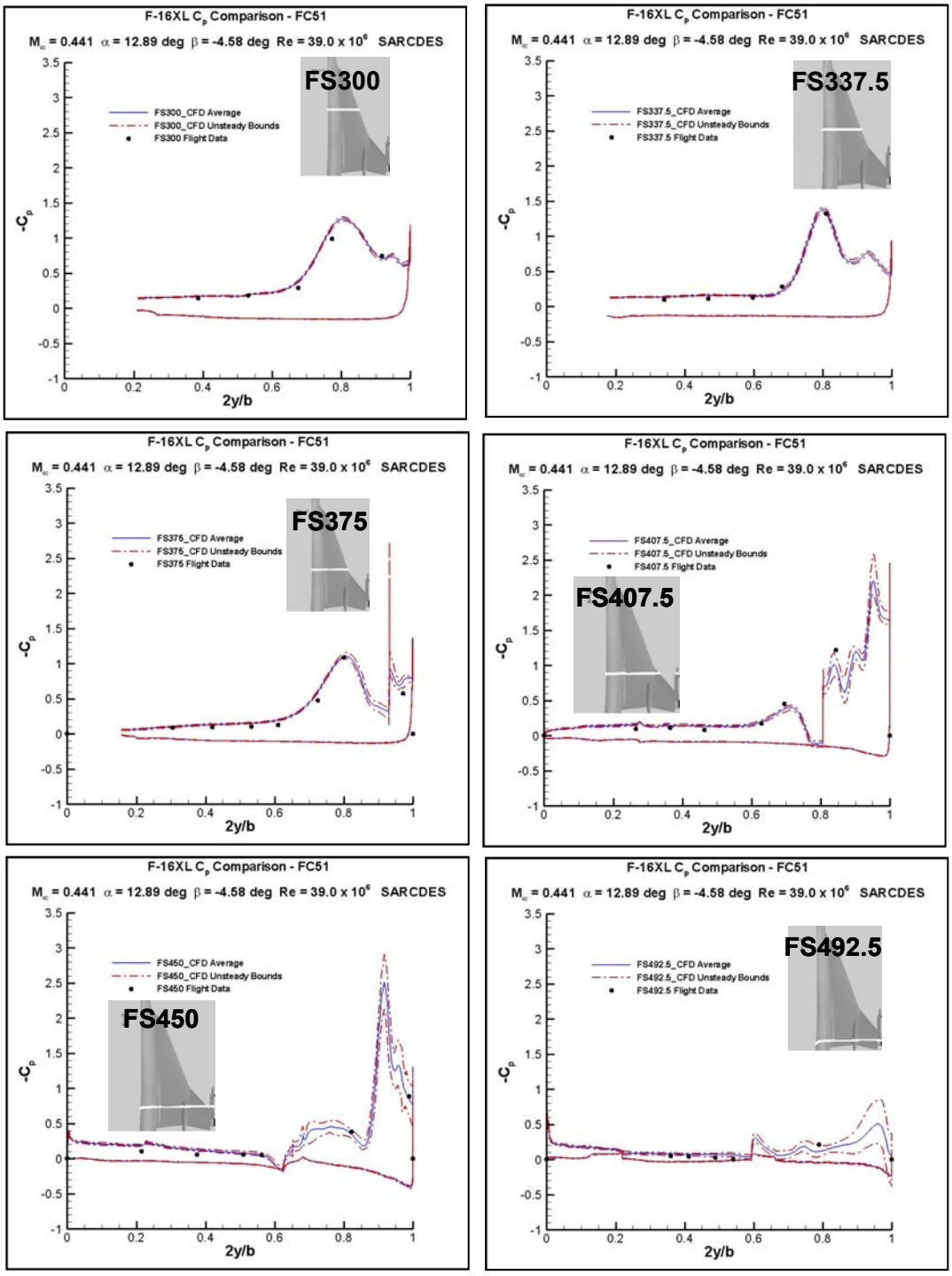

Figure 9-33: Flight Condition 51: Surface C_p along Various F-16XL Fuselage Stations (FS) for Flight Test, Computed Mean, and Computed Max and Min Values.

9.4.5 Improvements to the Baseline

This section describes modifications either to the flowfield conditions or the solver to account for differences between the computed data and the flight test data. The first improvement is to account for a non-zero sideslip in FC46 and the second is to incorporate recent improvements to the Detached-Eddy Simulation turbulence model.

9.4.5.1 Full Span FC46 Simulations

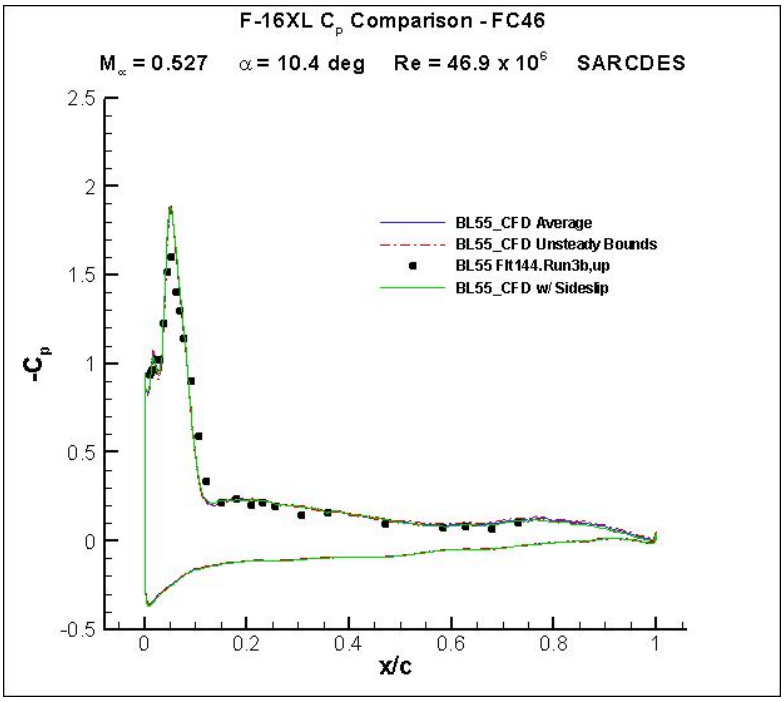

Figure 9-34: Flight Condition 46: F-16XL Surface C_p for Butt Line Station (BL) 55. Comparison between Flight Test and CFD solutions for assumed symmetry and a slight side slip to exactly match flight test.

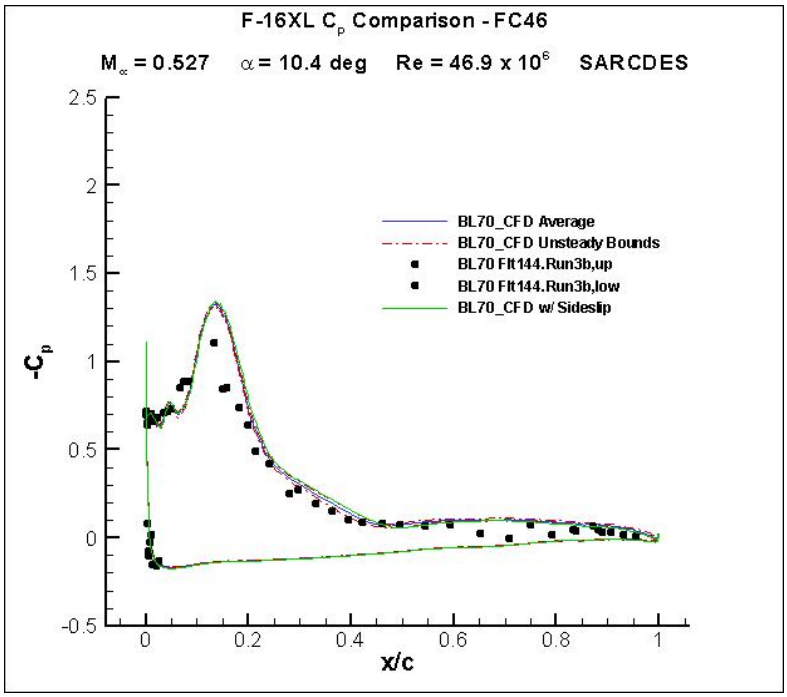

Figure 9-35: Flight Condition 46: F-16XL Surface C_p for Butt Line Station (BL) 70. Comparison between Flight Test and CFD solutions for assumed symmetry and a slight side slip to exactly match flight test.

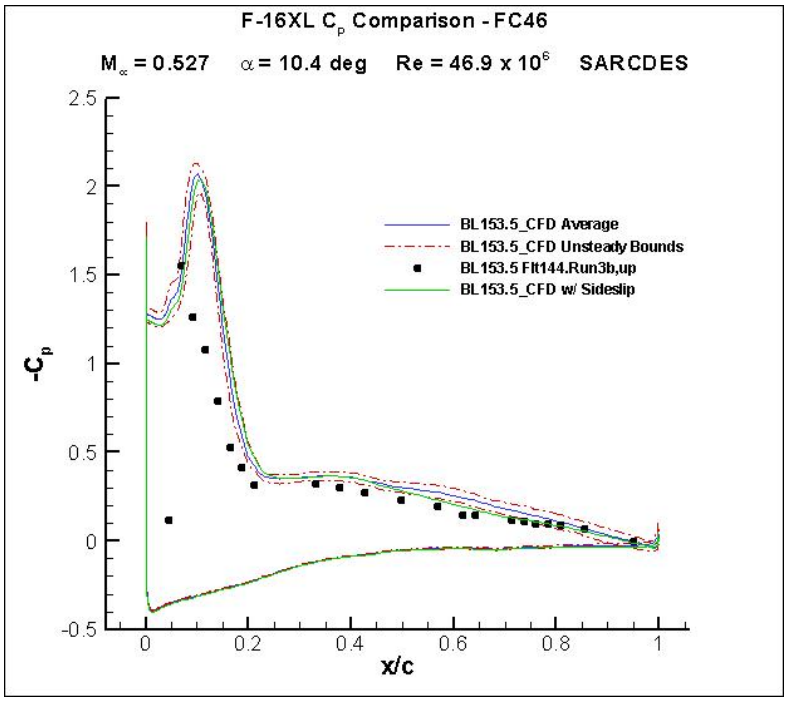

Figure 9-36: Flight Condition 46: F-16XL Surface C_p for Butt Line Station (BL) 153.5. Comparison between Flight Test and CFD solutions for assumed symmetry and a slight side slip to exactly match flight test.

9.4.5.2 Turbulence Model Improvements

Although the majority of comparisons were very good for the current unsteady solutions using the DES turbulence treatment, the boundary layer rake profiles of Rake 5 and 7 were disappointingly far from the flight test data. Since this mismatch was not evident in the C_p comparisons it was postulated that the differences may be due to the refined mesh near the leading edge creating an "embedded LES" region which is known to create incorrect boundary layer profiles [9-20]. This section presents solutions for an improved DES model called Delayed Detached Eddy Simulation (DDES) which delays the transition from RANS to LES to occur at the edge of the boundary layer. A complete discussion of the method is described in Reference [9-20].

Solutions were computed for Flight Condition 7 following the unsteady approach described in previous sections. Figure 9-37 depicts the comparison of C_p along BL 153.5 between DES and DDES turbulence treatments for both mean values and unsteady bounds of the simulation. It is clearly seen in the figure that the mean C_p values improved slightly to the flight test data for FC07. This improvement in C_p was consistent for all BL and FS data sets.

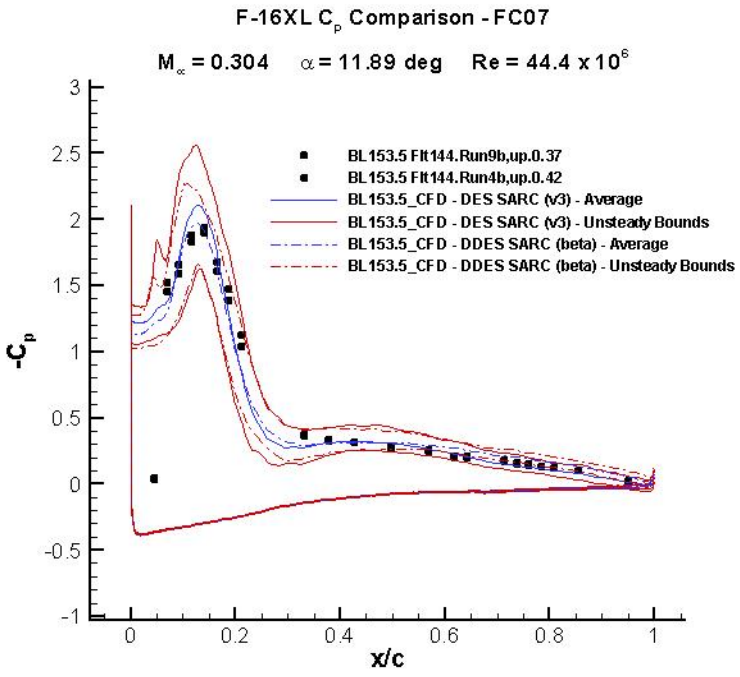

Figure 9-37: BL 153.5 C_p versus x/c for DES and DDES Turbulence Models and Flight Test.

The boundary layer rake profiles were also compared to determine if improvements were made with the DDES turbulence treatment. To review the issue, Rakes 3 and 4 compared well with experiments and CFD solutions from other CAWAPI participants. However, Rakes 5 and 7 significantly over predict the velocity ratio as a function rake height.

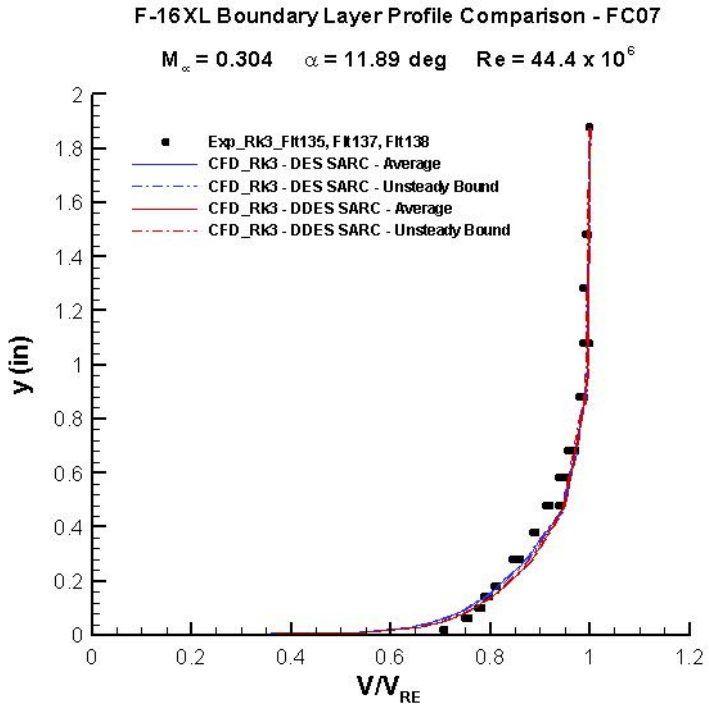

Figure 9-38: Rake 3 Boundary Layer Rake Velocity Scaled by Rake-Edge Velocity Profiles at Flight Condition 7. Mean and unsteady bounds for DES and DDES treatment solutions presented.

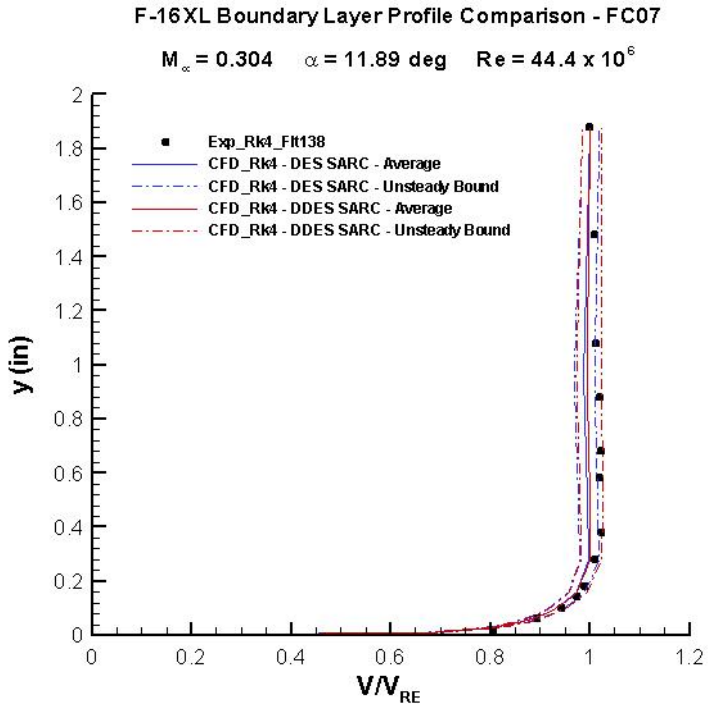

Figure 9-39: Rake 4 Boundary Layer Rake Velocity Scaled by Rake-Edge Velocity Profiles at Flight Condition 7. Mean and unsteady bounds for DES and DDES treatment solutions presented.

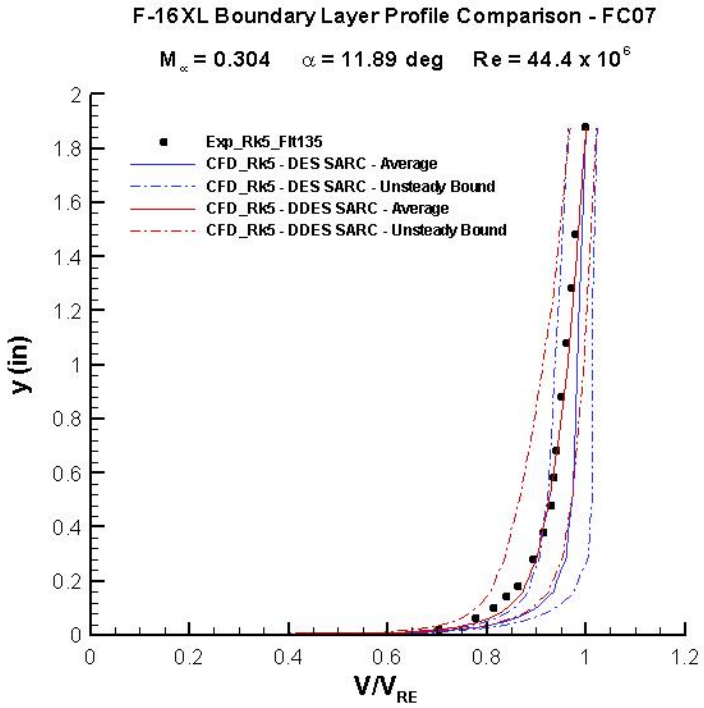

Figure 9-40: Rake 5 Boundary Layer Rake Velocity Scaled by Rake-Edge Velocity Profiles at Flight Condition 7. Mean and unsteady bounds for DES and DDES treatment solutions presented.

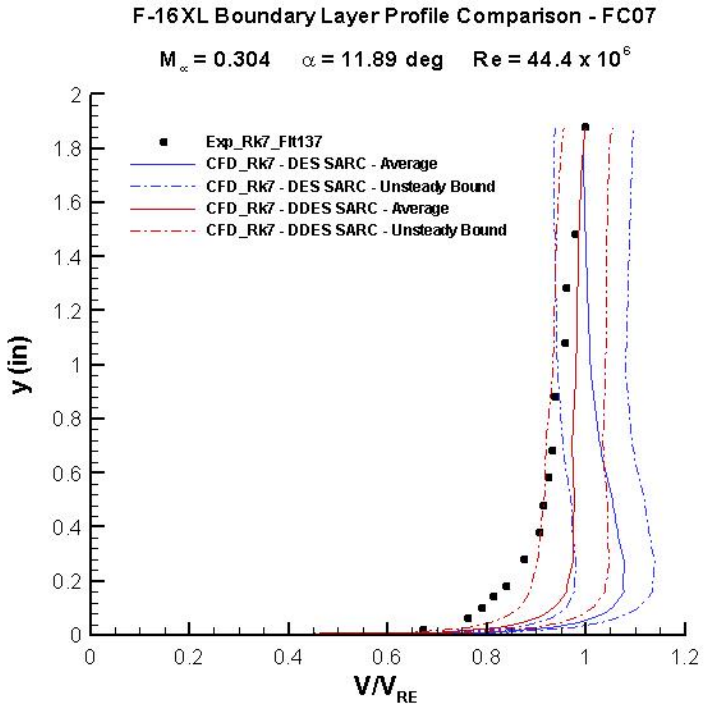

Figure 9-41: Rake 7 Boundary Layer Rake Velocity Scaled by Rake-Edge Velocity Profiles at Flight Condition 7. Mean and unsteady bounds for DES and DDES treatment solutions presented.

9.5 CONCLUDING REMARKS

Seven flight conditions of the F-16XL-1 aircraft were presented with comparisons to flight test data from the NASA CAWAP program. The ability of accurate CFD methods to compute and visualize these very complex vortical flowfields was evident and shown to be very useful for the aircraft industry. Very good agreement between surface C_p flight test data and computed data was seen in most subsonic cases. The unsteadiness of the simulations aft of vortex breakdown-like events were observed and quantified with min and max instantaneous C_p curves and compared to flight test, showing the utility of hybrid RANS-LES methods, such as DES, to compute these complex flowfields. The discrepancies for one of the rake boundary layer profiles and the surface skin friction data are subjects for further study and probably due to either miss-alignment of the velocity data in the case of the boundary layer velocity profile or grid refinement for both boundary layer and skin friction profiles.

9.6 REFERENCES

[9-1] Lamar, J.E., Obara, C.J., Fisher, B.D. and Fisher, D.F.: *Flight, Wind-Tunnel, and Computational Fluid Dynamics Comparison for Cranked Arrow Wing (F-16XL-1) at Subsonic and Transonic Speeds*, NASA TP-2001-210629, 2001.

[9-2] Lamar, J.E. and Obara, C.J.: *Review of Cranked-Arrow Wing Aerodynamics Project: Its International Aeronautical Community Role*, AIAA Paper 2007-0487, January 2007.

[9-3] Spalart, P.R., Jou, W-H., Strelets, M. and Allmaras, S.R.: *Comments on the Feasibility of LES for Wings, and on a Hybrid RANS/LES Approach,* Advances in DNS/LES, 1st AFOSR Int. Conf. on DNS/LES, August 4-8, 1997, Greyden Press, Columbus OH.

[9-4] Strang, W.Z., Tomaro, R.F. and Grismer, M.J.: *The Defining Methods of Cobalt: A Parallel, Implicit, Unstructured Euler/Navier-Stokes Flow Solver*, AIAA Paper 99-0786, January 1999.

[9-5] Forsythe, J.R., Hoffmann, K.A., Cummings, R.M. and Squires, K.D.: *Detached-Eddy Simulation with Compressibility Corrections Applied to a Supersonic Axisymmetric Base*, Journal of Fluids Engineering, Vol. 124, No. 4, 2002, pp. 911-923.

[9-6] Morton, S.A., Forsythe, J.R., Mitchell, A.M. and Hajek, D.: *Detached-Eddy Simulations and Reynolds-Averaged Navier-Stokes Simulations of Delta Wing Vortical Flowfields*, Journal of Fluids Engineering, Vol. 124, No. 4, 2002, pp. 924-932.

[9-7] Mitchell, A.M., Morton, S.A., Forsythe, J.R. and Cummings, R.M.: *Analysis of Delta-Wing Vortical Substructures Using Detached-Eddy Simulation*, AIAA Journal, Vol. 44, No. 5, 2006, pp. 964-972.

[9-8] Forsythe, J.R., Squires, K.D., Wurtzler, K.E. and Spalart, P.R.: *Detached-Eddy Simulation of Fighter Aircraft at High Alpha*, Journal of Aircraft, Vol. 41, No. 2, 2004, pp. 193-200.

[9-9] Forsythe, J.R. and Woodson, S.H.: *Unsteady Computations of Abrupt Wing Stall Using Detached-Eddy Simulation,* Journal of Aircraft, Vol. 42, No. 3, 2005, pp. 606-616.

[9-10] Morton, S.A., Cummings, R.M. and Kholodar, D.B.: *High Resolution Turbulence Treatment of F/A-18 Tail Buffet*, AIAA Paper 2004-1676, April 2004.

[9-11] Tomaro, R.F., Strang, W.Z. and Sankar, L.N.: *An Implicit Algorithm for Solving Time Dependent Flows on Unstructured Grids*, AIAA Paper 1997-0333, 1997.

[9-12] Grismer, M.J., Strang, W.Z., Tomaro, R.F. and Witzemman, F.C.: *Cobalt: A Parallel, Implicit, Unstructured Euler/Navier-Stokes Solver*, Adv. Eng. Software, Vol. 29, No. 3-6, pp. 365-373, 1998.

[9-13] Karypis, G., Schloegel, K. and Kumar, V.: *Parmetis: Parallel Graph Partitioning and Sparse Matrix Ordering Library*, Version 3.1, Technical Report, Dept. Computer Science, University of Minnesota, 2003.

[9-14] Samareh, S.: *GridTool: A Surface Modeling and Grid Generation Tool*, Proceedings of the Workshop on "Surface Modeling, Grid Generation, and Related Issues in CFD Solutions", NASA CP-3291, May 9-11, 1995.

[9-15] Pirzadeh, S.: *Progress Toward A User-Oriented Unstructured Viscous Grid Generator*, AIAA Paper 96-0031, 1996.

[9-16] *Cobalt Solutions*, Blacksmith User's Manual, Version 3.0, 2005.

[9-17] Gursul, I.: *Review of Unsteady Vortex Flows Over Delta Wings*, AIAA Paper 2003-3942, June 2003.

[9-18] Cummings, R.M., Morton, S.A. and Siegel, S.G.: *Computational Simulation and Experimental Measurements for a Delta Wing with Periodic Suction and Blowing*, Journal of Aircraft, Vol. 40, No. 5, 2003, pp. 923-931.

[9-19] Cummings, R.M., Morton, S.A., Siegel, S.G. and Bosscher, S.: *Numerical Prediction and Wind Tunnel Experiment for a Pitching Unmanned Combat Air Vehicle*, AIAA 41st Aerospace Sciences Meeting, Reno, NV, January 6-9, 2003. AIAA Paper 2003-0417.

[9-20] Travin, A.K., Shur, M.L., Spalart, P.R. and Strelets, M.: *Improvement of Delayed Detached-Eddy Simulation for LES with Wall Modeling*, European Conference on Computational Fluid Dynamics, 2006.